



TURKISH JOURNAL OF ENGINEERING

EDITOR IN CHIEF

Prof. Dr. Murat YAKAR
Mersin University Engineering Faculty
Turkey

CO-EDITORS

Prof. Dr. Erol YAŞAR
Mersin University Faculty of Art and Science
Turkey

Assoc. Prof. Dr. Cahit BİLİM
Mersin University Engineering Faculty
Turkey

Assist. Prof. Dr. Hüdaverdi ARSLAN
Mersin University Engineering Faculty
Turkey

ADVISORY BOARD

Prof. Dr. Orhan ALTAN
Honorary Member of ISPRS, ICSU EB Member
Turkey

Prof. Dr. Armin GRUEN
ETH Zurich University
Switzerland

Prof. Dr. Hacı Murat YILMAZ
Aksaray University Engineering Faculty
Turkey

Prof. Dr. Artu ELLMANN
Tallinn University of Technology Faculty of Civil Engineering
Estonia

Assoc. Prof. Dr. E. Çağlan KUMBUR
Drexel University
USA

TECHNICAL EDITORS

Prof. Dr. Ali AKDAĞLI
Dean of Engineering Faculty
Turkey

Prof. Dr. Roman KOCH
Erlangen-Nurnberg Institute Palaontologie
Germany

Prof. Dr. Hamdalla WANAS
Menoufyia University, Science Faculty
Egypt

Prof. Dr. Turgay CELIK
Witwatersrand University
South Africa

Prof. Dr. Muhsin EREN
Mersin University Engineering Faculty
Turkey

Prof. Dr. Johannes Van LEEUWEN
Iowa State University
USA

Prof. Dr. Elias STATHATOS
TEI of Western Greece
Greece

Prof. Dr. Vedamanickam SAMPATH
Institute of Technology Madras
India

Prof. Dr. Khandaker M. Anwar HOSSAIN
Ryerson University
Canada

Prof. Dr. Hamza EROL
Mersin University Engineering Faculty
Turkey

Prof. Dr. Ali Cemal BENİM
Duesseldorf University of Applied Sciences
Germany

Prof. Dr. Mohammad Mehdi RASHIDI
University of Birmingham
England

Prof. Dr. Muthana SHANSAL
Baghdad University
Iraq

Prof. Dr. Ibrahim S. YAHIA
Ain Shams University
Egypt

Assoc. Prof. Dr. Kurt A. ROSENTRATER
Iowa State University
USA

Assoc. Prof. Dr. Christo ANANTH
Francis Xavier Engineering College
India

Assoc. Prof. Dr. Bahadır K. KÖRBAHTI
Mersin University Engineering Faculty
Turkey

Assist. Prof. Dr. Akın TATOGLU
Hartford University College of Engineering
USA

Assist. Prof. Dr. Şevket DEMİRCİ
Mersin University Engineering Faculty
Turkey

Assist. Prof. Dr. Yelda TURKAN
Oregon State University
USA

Assist. Prof. Dr. Gökhan ARSLAN
Mersin University Engineering Faculty
Turkey

Assist. Prof. Dr. Seval Hale GÜLER
Mersin University Engineering Faculty
Turkey

Assist. Prof. Dr. Mehmet ACI
Mersin University Engineering Faculty
Turkey

Dr. Ghazi DROUBI
Robert Gordon University Engineering Faculty
Scotland, UK

JOURNAL SECRETARY

Nida DEMİRTAŞ
nidademirtas@mersin.edu.tr

TURKISH JOURNAL OF ENGINEERING (TUJE)

Turkish Journal of Engineering (TUJE) is a multi-disciplinary journal. The Turkish Journal of Engineering (TUJE) publishes the articles in English and is being published 3 times (January, May, September) a year. The Journal is a multidisciplinary journal and covers all fields of basic science and engineering. It is the main purpose of the Journal that to convey the latest development on the science and technology towards the related scientists and to the readers. The Journal is also involved in both experimental and theoretical studies on the subject area of basic science and engineering. Submission of an article implies that the work described has not been published previously and it is not under consideration for publication elsewhere. The copyright release form must be signed by the corresponding author on behalf of all authors. All the responsibilities for the article belongs to the authors. The publications of papers are selected through double peer reviewed to ensure originality, relevance and readability.

AIM AND SCOPE

The Journal publishes both experimental and theoretical studies which are reviewed by at least two scientists and researchers for the subject area of basic science and engineering in the fields listed below:

- Aerospace Engineering
- Environmental Engineering
- Civil Engineering
- Geomatic Engineering
- Mechanical Engineering
- Geology Science and Engineering
- Mining Engineering
- Chemical Engineering
- Metallurgical and Materials Engineering
- Electrical and Electronics Engineering
- Mathematical Applications in Engineering
- Computer Engineering
- Food Engineering

PEER REVIEW PROCESS

All submissions will be scanned by iThenticate® to prevent plagiarism. Author(s) of the present study and the article about the ethical responsibilities that fit PUBLICATION ETHICS agree. Each author is responsible for the content of the article. Articles submitted for publication are priorly controlled via iThenticate ® (Professional Plagiarism Prevention) program. If articles that are controlled by iThenticate® program identified as plagiarism or self-plagiarism with more than 25% manuscript will return to the author for appropriate citation and correction. All submitted manuscripts are read by the editorial staff. To save time for authors and peer-reviewers, only those papers that seem most likely to meet our editorial criteria are sent for formal review. Reviewer selection is critical to the publication process, and we base our choice on many factors, including expertise, reputation, specific recommendations and our own previous experience of a reviewer's characteristics. For instance, we avoid using people who are slow, careless or do not provide reasoning for their views, whether harsh or lenient. All submissions will be double blind peer reviewed. All papers are expected to have original content. They should not have been previously published and it should not be under review. Prior to the sending out to referees, editors check that the paper aim and scope of the journal. The journal seeks minimum three independent referees. All submissions are subject to a double blind peer review; if two of referees gives a negative feedback on a paper, the paper is being rejected. If two of referees gives a positive feedback on a paper and one referee negative, the editor can decide whether accept or reject. All submitted papers and referee reports are archived by journal Submissions whether they are published or not are not returned. Authors who want to give up publishing their paper in TUJE after the submission have to apply to the editorial board in written. Authors are responsible from the writing quality of their papers. TUJE journal will not pay any copyright fee to authors. A signed Copyright Assignment Form has to be submitted together with the paper.

PUBLICATION ETHICS

Our publication ethics and publication malpractice statement is mainly based on the Code of Conduct and Best-Practice Guidelines for Journal Editors. Committee on Publication Ethics (COPE). (2011, March 7). Code of Conduct and Best-Practice Guidelines for Journal Editors. Retrieved from http://publicationethics.org/files/Code%20of%20Conduct_2.pdf

PUBLICATION FREQUENCY

The TUJE accepts the articles in English and is being published 3 times. January, May, September a year.

CORRESPONDENCE ADDRESS

Journal Contact: tuje@mersin.edu.tr

CONTENTS

Volume 2 – Issue 3

ARTICLES

RHEOLOGICAL PARAMETER ESTIMATION OF CMC-WATER SOLUTIONS USING MAGNETIC RESONANCE IMAGING (MRI) <i>G. Bengusu Tezel</i>	94
INVESTIGATION OF Ni-Mn BASED SHAPE MEMORY ALLOY VARIATIONS TRANSFORMATION TEMPERATURES <i>Ece Kalay, Anil Erdağ Nomer and Mehmet Ali Kurgun</i>	98
INVESTIGATION OF DISSOLUTION KINETICS OF Zn AND Mn FROM SPENT ZINC-CARBON BATTERIES IN SULPHURIC ACID SOLUTION <i>Tevfik Agacayak and Ali Aras</i>	107
COMPARATIVE STUDY OF REGIONAL CRASH DATA IN TURKEY <i>Murat Özen</i>	113
PERFORMANCE COMPARISON OF ANFIS, ANN, SVR, CART AND MLR TECHNIQUES FOR GEOMETRY OPTIMIZATION OF CARBON NANOTUBES USING CASTEP <i>Mehmet Acı, Çiğdem İnan Acı and Mutlu Avcı</i>	119
INVESTIGATION OF ULEXITE USAGE IN AUTOMOTIVE BRAKE FRICTION MATERIALS <i>Banu Sugözü</i>	125
CRITICALITY CALCULATION OF A HOMOGENOUS CYLINDRICAL NUCLEAR REACTOR CORE USING FOUR-GROUP DIFFUSION EQUATIONS <i>Babatunde Michael Ojo, Musibau Keulere Fasasi, Ayodeji Olalekan Salau, Stephen Friday Olukotun and Ademola Mathew Jayeola</i>	130

Turkish Journal of Engineering



Turkish Journal of Engineering (TUJE)
Vol. 2, Issue 3, pp. 94-97, September 2018
ISSN 2587-1366, Turkey
DOI: 10.31127/tuje.363596
Research Article

RHEOLOGICAL PARAMETER ESTIMATION OF CMC-WATER SOLUTIONS USING MAGNETIC RESONANCE IMAGING (MRI)

G. Bengusu Tezel *¹

¹ Abant Izzet Baysal University, Faculty of Engineering and Architecture, Department of Chemical Engineering,
Bolu, Turkey
ORCID ID 0000-0002-0671-208X
gulerbengusutezel@ibu.edu.tr

* Corresponding Author

Received: 07/12/2017 Accepted: 20/01/2018

ABSTRACT

In this study, the application of Magnetic Resonance Imaging (MRI) rheometry on the measurement of complex fluid Carboxymethyl cellulose (CMC)-water solutions (0.5%, 1.0%, 1.5%, 2.0% w/w) flow was described. Depending on CMC concentration, Power law or Herschel-Bulkley models gave the best fit according to MRI and conventional rheometer (CVO) results. Power Law model was valid for 0.5% and 1.0% CMC ($R^2=0.9993$ - $R^2=0.9987$ and $R^2=0.9983$ - $R^2=0.9985$ respectively by MRI and CVO). On the other hand, 1.5% and 2.0% CMC solutions flow were well described by Herschel-Bulkley model ($R^2=0.9994$ - $R^2=0.9996$ and $R^2=0.9986$ - $R^2=0.9981$ respectively by MRI and CVO). The MRI measurements agreed well with the CVO measurements.

Keywords: *Magnetic Resonance Imaging, Conventional Rheometer, CMC, Rheology*

1. INTRODUCTION

Offline methods for rheological measurements such as cylindrical coquette, cone and plate geometries (conventional rheometries) generally used for the study of fluid motion in shear. However, obtained results from these types of geometries need to be verified with suitable online or inline methods. Especially, many industrial processes, such as extrusion, transfer processes involve established or developing flows in pipes or tubes. Therefore, online techniques based on the measurement of the velocity profile in a pipe flow using Magnetic Resonance Imaging (MRI), which is a non-invasive method, and simultaneously determining the pressure drop, are promising for use a product quality or rheology control tool during the fluid flow. Magnetic resonance imaging (MRI) can be used as a viscometer, based on analysis of a measured velocity profile of fluid flowing in a tube coupled with a simultaneous measurement of the pressure drop driving the flow (Arola *et al.*, 1997 and Arola *et al.*, 1999). This type of measurement is well suited for rheological characterization of non-Newtonian fluids (Choi *et al.*, 2002 and Tozzi *et al.*, 2012).

To evaluate shear viscosity in tube (or capillary) flow, an incompressible fluid must undergo steady pressure-driven flow in the laminar regime. The conservation of linear momentum, which equates pressure forces to viscous forces, provides the relationship between the shear stress, σ , and radial position, r :

$$\sigma(r) = \frac{-\Delta P}{2L} r \quad (1)$$

where ΔP is the pressure drop over the tube length L . The shear rate is obtained at the same radial position using the velocity profile obtained from a flow image. The expression for the shear rate in tube flow is:

$$\gamma(r) = \frac{dV(r)}{dr} \quad (2)$$

Where V is the axial velocity. Using Equations 2 and 3, the apparent viscosity η is determined by the ratio of shear stress to shear rate:

$$\eta(r) = \frac{\sigma(r)}{\gamma(r)} \quad (3)$$

Graphical User Interface (GUI) programs are used to analyze data and display rheological results (Choi *et al.*, 2005 and Tozzi *et al.*, 2012). Main step in the data processing procedure include calculating the shear stress as a function of radial position in the pipe, processing the velocity profile image to obtain a velocity profile, calculating the shear rate as a function of radial position from the velocity profile, and generating the rheogram by plotting the shear stress against the shear rate (Arola *et al.*, 1997, Callaghan 1999 and Tozzi *et al.*, 2012). Calculating the shear stress is straightforward as in Equation 1.

In this study, Carboxymethyl cellulose (CMC) was used as test fluid. CMC is widely used as thickener

especially in food and pharmaceutical industries (Benchabane and Bekkour, 2008). This is also known as complex fluid due to no linear relationship between stress and shear rate in simple shear during the flow.

2. MATERIALS AND METHODS

2.1. Materials

The CMC, with nominal molecular weight of 250,000 g/mol was supplied from Sigma. Aqueous solutions of CMC were prepared by dissolving the appropriate amount of CMC powder in distilled water. The high CMC concentration solutions (0.5%, 1.0%, 1.5%, 2% w/w.) were prepared by using water heated at 50 °C by gentle stirring with the sufficient time < 24 h.

Online and offline measurements were performed with an MRI (Magnetic Resonance Imaging) at Food and Science Technology Department at University of California, Davis, USA using flow loop depicted in Fig. 1. At 25 °C, MRI Flow Imaging Tests were done for 0.5, 1, 1.5, 2% (w/w) CMC solutions to determine rheological constitutive equations parameters. Inlet diameter of PVC tube was 38.1 mm. The test fluid was recirculated using Moyno pump (Integrated Motor Drive System, Franklin Electric) Pressure drop was obtained at the ends of pipe with a constant length of 1.68 m using pressure transducer (Siemens Company).



Fig. 1. Flow loop setup for CMC testing A) Positive displacement pump B) MRI magnet

2.2. Methods

In Fig. 2, flow image for an example of 0.5% CMC flow, can be seen with data processing window. The velocity profile is used to obtain shear rate distribution, while the pressure drop is used to calculate the shear stress distribution. By taking the ratio of these quantities at a radial position, local viscosity can be obtained within the shear rate range in the flow, zero at the center, and maximum at the wall, within minutes. There is not observed slip effect on the wall as in Fig. 2.

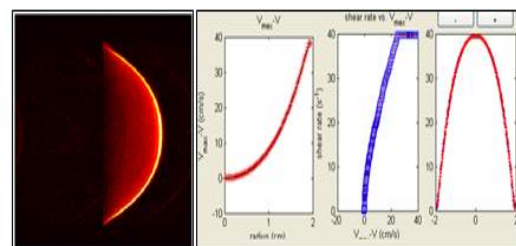


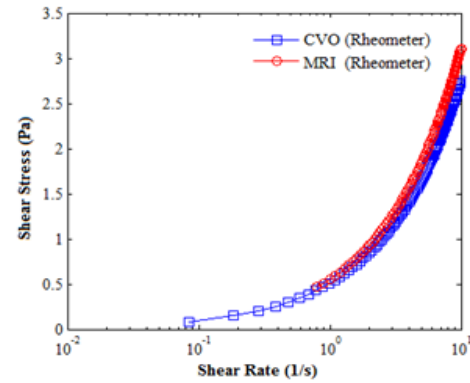
Fig. 2. MRI Image for 0.5% CMC

Fig. 2 shows the flow curves of the CMC solutions at different concentrations. Instrument CVO rheometer (Bohlin Instruments) with a cone and plate rheometer (with a cone angle 4° and diameter 40 mm) at 25 °C was used for offline measurement. A steady state shear rate ramp from 0.085 to 10 s⁻¹ was performed in logarithmic mode with 10 points/decade.

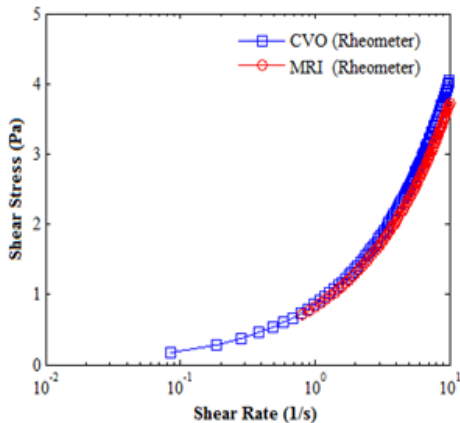
3. RESULTS AND DISCUSSIONS

For MRI measurements at the different pump speed of flow loop and also measured using a conventional technique and the agreement between the results is satisfactory shown in Figure 3. MRI measurement results of CMC solutions are also listed in the Table 1 with changing pump speed of flow loop shown in Fig. 3.

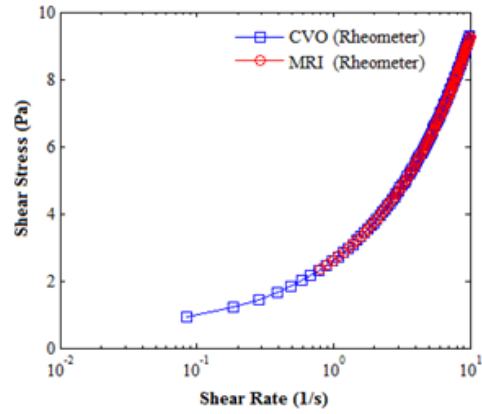
All obtained rheograms for different CMC solutions are as listed in Table 1. Rheological properties are independent of flow velocity. Hence, zero shear viscosities are nearly constant during the flow. As Reynolds number and concentration of flow increased, fluid shear stress acting on the pipe wall also increased as seen in Table 1.



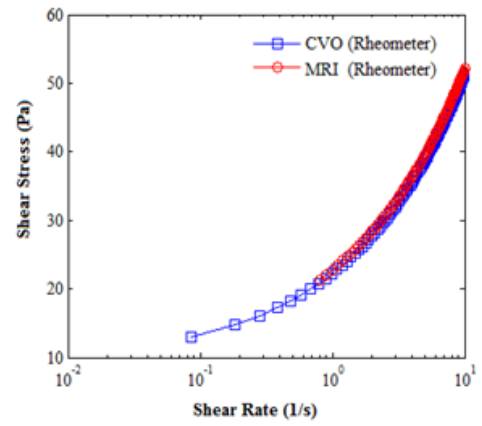
(a)



(b)



(c)



(d)

Fig. 3. Flow curves of shear stress versus shear rate for CMC- water for various mass fractions (a) 0.5% CMC (b) 1.0% CMC (c) 1.5% CMC (d) 2.0% CMC) at 25 °C

Rheological parameters for CMC solutions are also listed in Table 2. Depending on CMC concentration, Power law or H.Bulkley models give the best fit according to MRI flow result using Equations 4 and 5 respectively. Power Law model is valid for 0.5% and 1.0% CMC. On the other hand, 1.5% and 2.0% CMC solutions flow are well described by Herschel–Bulkley model.

$$\sigma = K\gamma^n \quad (4)$$

$$\sigma = \sigma_0 + K\gamma^n \quad (5)$$

Table 1. MRI flow measurement for CMC-water solutions

	Pump Speed (rpm)	V(m/s)	Re	Wall stress (Pa)	Zero Shear Viscosity (Pa.s)
0.5% CMC	330	0.023	2.176	4.371	0.412
	400	0.039	4.020	4.840	0.411
	700	0.078	8.840	7.590	0.411
	1000	0.121	14.445	11.730	0.413
1.0% CMC	1500	0.196	25.013	15.240	0.415
	330	0.032	1.620	7.230	1.002
	430	0.043	2.312	9.350	1.003
	600	0.060	3.390	12.780	1.001
	1000	0.122	7.870	20.670	1.002
	1500	0.193	13.590	28.605	1.001
1.5% CMC	330	0.035	0.970	16.800	2.001
	460	0.047	1.400	21.560	1.989
	600	0.058	1.850	27.770	2.012
	1000	0.094	3.300	42.540	2.014
	1500	0.183	7.690	55.550	2.001
2.0% CMC	330	0.031	0.180	53.681	9.012
	500	0.053	0.360	77.670	9.022
	800	0.077	0.580	95.431	8.912
	1000	0.095	0.760	106.071	8.993
	1500	0.147	1.340	127.350	8.912

In Equations 4 and 5, consistency index, K , and power law index, n , and yield stress, σ_0 , data values are obtained from shear stress v.s. shear rate data using online (MRI Rheometry) method and offline (CVO Rheometry) method. R^2 values of the fittings are also satisfactory. As CMC concentration increased, yield stress gets larger and elastic forces dominates the viscoelastic flow medium (Nguyen & Boger, 1992).

Table 2. Rheological Parameters for CMC-water solutions

	MRI Rheometer	CVO Rheometer	Goodness of the fit R^2 (MRI- CVO)
0.5% CMC	$K=0.550$ $n=0.753$	$K=0.512$ $n=0.730$	0.9993-0.9987
1.0% CMC	$K=0.825$ $n=0.653$	$K=0.863$ $n=0.670$	0.9983-0.9985
1.5% CMC	$\tau_0=0.436$ $K=2.176$ $n=0.607$	$\tau_0=0.424$ $K=2.640$ $n=0.608$	0.9994-0.9996
2.0% CMC	$\tau_0=9.054$ $K=14.731$ $n=0.495$	$\tau_0=9.150$ $K=13.120$ $n=0.507$	0.9986-0.9991

4. CONCLUSION

MRI velocity measurements with a pressure drop measurements allows a relationship between shear rate and shear stress and yields a rheological parameters measurements. A rheological investigation of CMC flow of 0.5%, 0.10%, 0.15%, 0.20% w/w concentrations in

MRI and CVO was presented. The following conclusions can be highlighted from the results of the study:

- Rheological parameters are independent of flow conditions.
- 0.5% and 1.0% w/w CMC are suited with Power law model. 1.5% and 2.0% CMC w/w solutions flow are well described by Herschel–Bulkley model.
- Online and offline measurement results are good agreement with each other.
- MRI flow imaging is suitable for evaluations of rheological parameters of CMC solutions even in high concentration of 1.5 and 2.0% w/w CMC.

REFERENCES

- Arola, D.F., Barrall, G.A., Powell, R.L., McCarthy, K.L. and McCarthy, M.J., (1997). "Use of nuclear magnetic imaging as a viscometer for process monitoring." *Chem. Eng. Sci.*, Vol. 52, No. 13, pp 2049–2057.
- Arola, D. F., Powell, R. L., Barrall, G. A. and McCarthy, M. J. (1998). "A simplified method for accuracy estimation of nuclear magnetic resonant imaging." *Rev. Sci. Instrum.* Vol. 69, No. 13, pp. 3300–3307.
- Arola, D. F., Powell, R. L., Barrall, G. A. and McCarthy, M. J. (1999) "Pointwise observation for rheological characterization using nuclear magnetic resonance imaging." *J. Rheol.* Vol. 43, No. 1, pp. 9–30.

Benchabane, A. and Bekkour, K. (2008). "Rheological properties of carboxymethyl cellulose (CMC) solutions." *Colloid Polym. Sci.* Vol. 286, No. 10, pp.1173–1180.

Callaghan, P. T. (1999). "Rheo-NMR: nuclear magnetic resonance and the rheology of complex fluids." *Reports Prog. Phys.* Vol. 62, No. 4, pp. 599–670.

Choi, Y. J., McCarthy, K. L. and McCarthy, M. J. (2005) "A MATLAB graphical user interface program for tomographic viscometer data processing." *Comput. Electron. Agric.* Vol. 47, No. 3, pp.59–67.

Nguyen, Q. D. and Boger, D. V. (1992). "Measuring the flow properties of yield stress fluids." *Annu. Rev. Fluid Mech.* Vol. 24, No. 1, pp. 47–88.

Tozzi E.J., Bacca L.A., Hartt W.H., McCarthy, K.L. and M.J. McCarthy (2012). "Robust processing of capillary velocimetry data via stress-rescaled velocity functions." *J. Rheol.*, Vol. 56, No. 6, pp. 1464-1499.

ACKNOWLEDGEMENTS

Authors would like to thank Prof. Dr. Micheal J. McCarthy for his help and open his laboratory in Food Science and Technology Department, UC, Davis, USA.

Copyright © Turkish Journal of Engineering (TUJE). All rights reserved, including the making of copies unless permission is obtained from the copyright proprietors.

Turkish Journal of Engineering



Turkish Journal of Engineering (TUJE)
Vol. 2, Issue 3, pp. 98-106, September 2018
ISSN 2587-1366, Turkey
DOI: 10.31127/tuje.374215
Research Article

INVESTIGATION OF Ni-Mn BASED SHAPE MEMORY ALLOY VARIATIONS TRANSFORMATION TEMPERATURES

Ece Kalay ^{*1}, Anıl Erdağ Nomer ² and Mehmet Ali Kurgun ³

¹ Mersin University, Engineering Faculty, Department of Mechanical Engineering, Mersin, Turkey
ORCID ID 0000-0003-2470-7791
eecekalay@gmail.com

² Mersin University, Engineering Faculty, Department of Mechanical Engineering, Mersin, Turkey
ORCID ID 0000 – 0002 – 8997 – 6936
erdagnomer@hotmail.com

³ Mersin University, Engineering Faculty, Department of Mechanical Engineering, Mersin, Turkey
ORCID ID 0000 – 0001 – 5565 – 1351
malikurgun@gmail.com

* Corresponding Author

Received: 03/01/2018

Accepted: 25/02/2018

ABSTRACT

Shape memory alloys' usage frequency and areas are increased day to day. It is seen the different type and different characteristics in many industrial areas. Therefore, shape memory alloys, which are intelligent materials, are very fast to develop. The NiTi alloys, from these alloy types, are most commonly used due to their low hysteresis range and biocompatibility. But production costs and difficulties have led, investigators to investigate different alloy types. Shape memory alloys which produced with possibly cheaper elements, examined in researchers with looking at their transformation temperatures.

Keywords: *Dsc, NiTi, Shape Memory Alloys*

1. INTRODUCTION

Shape memory alloys (SMA) are materials known as intelligent metals from the past to present day. In the past, SMA's found in various composition ratios of constrained elements are alloyed with many elemental ingredients now (Canbay, 2017). SMA's shed light on future systems and applications at a high level. The technologies that will be developed with unique features will provide great advantages and their usage will be necessary. High strength, biocompatibility, high wear resistance, high corrosion resistance, working in high temperature and pressure, elasticity ductility etc. intelligent metal alloys are made depending on the needs of the sectors. Healthcare field, defense, and military fields, mechanical systems, automotive sectors etc. (Canbay *et al.*, 2014; Canbay, 2017; Canbay *et al.*, 2017; Canbay *et al.*, 2018). SMA's are required to be developed and used in the fields. Producing SMA's according to the needs of the areas to be used will be the best course of approachment. In order to meet the requirements of the application areas of SMA materials, the alloys must be full-featured and very diverse. Once the SMA's are approached, technology and sectors will be advantageous and the work on these intelligent materials will become more important. The SMA's are a very valuable issue for the Research & Development area. Considering the advantages and convenience of intelligent materials, it is a bright field of materials that many industries in the manufacturing and the business world will not spare their investments and supports (Eskil *et al.*, 2015). SMA's have a certain high temperature phase and low temperature phase according to their element proportion that they contain. The high temperature phase is called the austenite phase, the low temperature phase is called the martensite phase. According to the phase temperature limits, it is determined at which temperature degree the shape memory conversion. This phase change is due to solid-state phase change. In general, the memory-trained shape will talk about memory formation; The SMA material is subjected to shape training. This is another issue that needs to be addressed in more detail (Ozkul *et al.*, 2017). However, in the rough description of the work, the shape desired to be taken into memory is usually placed in a mold and heated to a high temperature austenite phase under tension. The alloyed material is converted to the low temperature martensite phase by shock cooling after heating to the austenite phase (Aldas *et al.*, 2014). This cycle is repeated according to the type of material and the methods have differed one-way or two-way. After this process, the SMA will save it in the memory, which is determined in advance of the applied processes. After this step, heat, stress, or both subjected to the plastic deformation that has been exposed and the shape changes back to the SMA as it was recorded in the memory when heated from high to the high temperature austenite phase. It takes its place in the group of intelligent materials (Canbay *et al.*, 2014). It has been stated that the SMA's have various advantageous properties according to the proportion of the elements they contain. Today, many test and screening systems are used in determining these properties. The most common of these is the differential scanning calorimetry (DSC). The DSC test is an important test for determining the temperature points and boundaries of the austenite and martensite phases, which are very important in the

memory acquisition of SMA's. The results of DSC scanning of various alloys of elements such as nickel, manganese, gallium, iron, aluminum, and tin have been examined in the literature review. The start and finish temperatures of the austenite and martensite phases were determined. The effect of element contents on phase transformation temperatures was investigated (Aldas *et al.*, 2016).

The austenite-initiation temperature (A_s) is the temperature at which this transformation begins, and the austenite-final temperature (A_f) is the temperature at which this transformation is complete. When the SMA heats up, the contract starts and returns to its original state. This conversion is possible even at high applied loads and, therefore, results in a high energy density of the trigger. During the cooling process, the transformation starts at the martensite starting temperature (M_s) and completes when the martensite reaches the finishing temperature (M_f) (Buehler *et al.*, 1963). Martensite is called the highest temperature M_a that can be caused by residual stress, and when it is above this temperature, SMA permanently deforms like ordinary metallic materials (Duerig *et al.*, 1994). These deforming effects, known as SMA and pseudo elasticity (or super elasticity), can be categorized according to three-dimensional memory properties:

- One-way shape memory effect (OWSME): The unidirectional SMA (SMA) maintains a deformed condition after removing an external force and then returns to its original state upon heating.
- Two-way shape memory effect (TWSME) or reversible SME: In addition to the one-sided effect, bi-directional SMA (TWSMA) can remember both high and low temperature shape. Often the recovery provided by OWSMA for the same material (Schroeder *et al.*, 1977; Huang *et al.*, 2000) yields about half of the water, and this stress tends to deteriorate quickly, especially at high temperatures (Ma *et al.*, 2010). For this reason, OWSMA offers a more reliable and economical solution (Stöckel 1995).
- Pseudo elasticity (PE) or Super elasticity (SE): The SMA returns to its original shape after applying the mechanical load without the need for any thermal activation at temperatures between A_f and M_a .

In addition to the TWSME material above, the prejudicial OWSMA actuator can also function as a 'mechanical TWSME' at a macroscopic (structural) level; more robust, reliable, and widely applied in many engineering applications (Sun *et al.*, 2012). This feature is important and should be considered carefully when selecting SMA materials for targeted applications. For example, a small hysteresis is needed for applications where rapid movement is necessary (robotic applications) (Liu, 2010). The physical and mechanical properties of some SMAs also vary between these two phases, such as Young's modulus, electrical resistance, thermal conductivity, and thermal expansion coefficient (Mihálcz, 2001; Mertmann *et al.*, 2008; Sreekumar *et al.*, 2009). The austenite structure is rigid and has a high Young's modulus. The martensite structure is softer. It can easily deform with the external load (Hodgson *et al.*, 1990; Mihálcz, 2001).

There are three varieties of SMA. These alloys are listed in the literature as NiTi, copper based and iron

based. The most capable of these alloy types is NiTi alloys. Because these alloy types have biocompatibility, they are used in many fields, especially in the field of medicine. Copper-based SMA is the closest to this type of alloy. But there is no popular. Iron-based SMA is the weakest type in this group because they have high hysteresis. In our study, the data of alloy types which may be alternative to NiTi-based SMA will be examined. The temperature transformation points of the austenite and martensite phases of the samples were determined and analyzed on the table and the thermal properties of the shape memory alloys were obtained. All text should be left and right justified. Footnotes and underlines are not allowed.

2. LITERATURE REVIEW

The starting and ending temperatures of the austenite high temperature phase and the martensite low temperature phase are determined and tabulated in the literature review. The bibliographic numbers of the literature search of the thermal values of SMA's are listed at the beginning of the table as (Kainuma *et al.*, 1996; Jiang *et al.*, 2002; Jiang *et al.*, 2003; Wu *et al.*, 2003; Koho *et al.*, 2004; Lanska *et al.*, 2004; Glavatsky *et al.*, 2006; Koyama *et al.*, 2006; Babita *et al.*, 2007; Santos *et al.*, 2008; Aksoy *et al.*, 2009; Wu *et al.*, 2011; Zheng *et al.*, 2011; Turabi *et al.*, 2016; Caputo *et al.*, 2017; Mostafaei *et al.*, 2017). The transformation temperatures obtained by different element contributions of Ni and Mn-based SMA materials are shown in Table 1.

2.1. Evaluation of Literature Review

In the direction of information from the source if we evaluate the change of austenite and martensite starting end temperature points by changing atomic ratios of nickel, manganese and aluminum elements, In the first sample, nickel and manganese were alloyed at 50 percent and specific temperature points were obtained. It has been observed that the austenite and martensite phase change temperatures are lowered when aluminum is added to this alloy and the manganese proportion is reduced (with the nickel ratio being kept constant). It is observed that when the aluminum ratio is kept constant and the nickel ratio is increased and the manganese ratio is decreased, the phase change temperatures are increased (Kainuma *et al.*, 1996).

Increasing the tin ratio in nickel, manganese and tin alloys has clearly reduced the phase conversion temperature (Koyama *et al.*, 2006; Santos *et al.*, 2008; Zheng *et al.*, 2011; Turabi *et al.*, 2016).

Nickel, manganese and antimony triple alloys have been investigated, and when the antimony ratio in the alloy is reduced, the transformation temperatures of the austenite and martensite phases have increased at a high rate. As a result of this observation, antimony addition reduces the high conversion temperatures (Aksoy *et al.*, 2009).

Nickel, manganese, and gallium ternary alloys were added to the dysprosium element and the effects on the temperature values were observed. When the dysprosium element increased, the phase transformation temperatures increased (Babita *et al.*, 2007).

Nickel, manganese, gallium triple alloy system is added to the silicium element. As the silicium ratio increased, the phase transformation temperatures

decreased. When cobalt element is added instead of silicium, cobaltite phase transformation temperatures are lowered in the same way and the austenite and martensite start-finish transformation temperatures are increased by increasing the nickel ratio (Glavatsky *et al.*, 2006).

Table 1. Transformation temperatures obtained by different element contributions of Ni and Mn based shape memory alloy materials

Ref.	Ni (at.%)	Mn (at.%)	Ga (at.%)	Fe (at.%)	In (at.%)	Si (at.%)	Co (at.%)	Dy (at.%)	Al (at.%)	Sn (at.%)	Sb (at.%)	In (at.%)	Co (at.%)	M _s (°C)	M _f (°C)	A _s (°C)	A _f (°C)
(Wu and Yang, 2003)	50,19	24,71	25,1											-118,5	-126,6	-106	-85
	50,69	23,07	26,24											-146,1	-148,5	-142	-132
	50,33	23,87	25,8											-116,2	-151,3	-132	-124
	50,33	24,38	25,29											-115,5	-129,5	-100	-88
	50,49	24,22	25,28											-76,5	-89,4	-65	-50
	50,28	24,77	24,96											-79,3	-86,6	-69	-60
	50,34	24,8	24,86											-69,3	-80,8	-60	-50
	50,36	24,88	24,75											-65,2	-85,3	-58	-45
	50,56	24,57	24,87											-70,1	-87,5	-59	-43
	50,61	24,84	24,55											-41,9	-58,2	-38	-22
	50,41	25,26	24,33											-55,7	-72,2	-47	-36
	51,56	23,43	25,02											-33,9	-50,4	-23	-9
	51,12	24,3	24,58											-48,8	-61,4	-47	-32
	51,93	23,07	25,01											-32,9	-47,8	-22	-5
	50,98	24,83	24,19											-27,5	-38,5	-17	-6
	50,4	25,85	23,75											-33,1	-45,4	-24	-16
	51,27	24,49	24,24											-16,5	-33,4	-8	12
	51,38	24,81	23,81											-2	-12,2	4	20
	51,19	25,2	23,73											12,5	-17	16	35
	52,84	22,44	24,72											2,7	-13,8	14	28
	53,23	21,85	24,92											7,1	-4,3	20	31
	50,46	26,74	22,8											-7,8	-19,3	6	13
	51,71	24,84	23,45											22,9	5,3	24	40
	50,39	27,77	21,84											26	15,7	30	42
	52,29	24,59	23,12											37,6	30,4	46	50
	52,14	25,16	22,67											58,4	38,8	64	82
	52,54	24,78	22,68											59,4	41,4	53	73
	52,63	24,73	22,64											54,5	40	58	74
55,78	19,52	24,7											92,2	74,8	102	120	

	50,48	28,87	20,65											66	36,8	47	76
	52,84	24,82	22,34											74,3	54,3	68	88
	53,45	24,07	22,48											77,6	55,8	82	104
	53,26	24,68	22,06											100,7	66,7	100	121
	50,37	29,79	19,84											82,2	63,5	80	98
	53,64	24,56	21,82											114,7	80,6	124	135
	53,71	25,27	21,02											158,5	117,2	143	177
	54,15	24,88	20,97											185,3	178,6	202	217
(Jiang <i>et al.</i> , 2002)	53	25	22											109	97	116	134
(Jiang <i>et al.</i> , 2003)	53	22	25											-4	-14	2	16
(Babita <i>et al.</i> , 2007)	50	29	20,9					0,1						66,1	58,9	63	71
	50	29	20,5					0,5						71,2	66,2	71	76
	48	29	20					1						75,9	-28,2	76	80
	49	29	19					2						126,2	116,3	124	132
(Glavatsky <i>et al.</i> , 2006)	47,9	26,1	26											39	38	52	52
	49,7	28,7	21,6											32	30	38	41
	50,5	28,2	21,3											38	34	41	47
	51,4	27,2	21,4											78	72	80	86
	49,9	28	21,6				0,5							17	12	20	25
	50	28,8	20,6				0,6							28	-10	-3	36
	50,4	28,8	19,8				1							25	-5	3	32
	49,6	27,7	20,6				2,1							-128	-136	-111	-103
	48,6	24,8	22,9		3,4									6	-17	-3	16
	51,7	28,5	15,6		4,2									-95	-105	-73	-70
	46,6	25,8	26,8					1,7						-7	-12	-6	0
	43,5	27,9	22,8					5,8						-56	-60	-51	-46
	50	29	18,8					2,2						223	211	224	237
	47,3	25,9	20,4	6,4										13	1	20	30
	49,4	27,5	21,3	1,8										43	39	54	59
	50,9	20,2	23,7	5,2										7	2	6	13
	51,3	14,4	26,3	8										86	79	88	101
51,8	24,3	23,2	0,7										29	11	21	31	
52,1	23	24,2	0,7										30	0	20	25	

(Koho <i>et al.</i> , 2004)	51,7	24,4	22,7	1,2										53	34	41	62
	47,3	30,3	20,3	2,1										53	32	42	61
	48,9	29	19,5	2,6										65	52	53	76
	48,8	29,2	20,1	1,9										45	27	49	64
	48,6	27,5	21,6	2,3										31	22	33	41
	48,9	26,2	22,6	2,3										57	45	58	70
	49,4	27,9	20,3											54	42	54	59
	50,2	27,4	21,1											61	50	63	77
	49,6	28,3	20,7											53	36	48	64
	50,1	28,2	20,9	0,8										44	28	40	64
	49,2	29,6	21,2											31	28	35	38
	52,2	27,3	20,6											132	112	102	122
(Lanska <i>et al.</i> , 2004)	50,7	28,4	20,9											61	52	66	72
	50,7	28,3	21											57	50	65	70
	50,7	27,8	21,5											52	50	58	61
	50,6	28,5	20,9											60	58	66	68
	50	29,8	20,2											71	67	74	78
	50	28,9	21,1											48	38	47	57
	49,9	29,9	20,2											71	65	77	81
	49,7	29,1	21,2											38	36	46	48
	49,6	29,2	21,2											30	28	36	36
	49,2	30,6	20,2											55	50	60	64
	49,1	30,7	20,2											51	48	59	62
	49	30,3	20,7											39	36	45	50
	48,5	30,3	21,2											29	26	32	35
	51	28,5	20,5											83	77	81	87
	50,5	29,4	20,1											78	70	75	84
	49,5	30,3	20,2											68	64	71	75
	48,8	31,4	19,8											64	60	65	69
	54,9	23,8	21,3											286	268	295	314
	54	24,7	21,3											224	214	225	237
	53,9	24,4	21,7											257	251	278	287
53,7	26,4	19,9											250	239	265	273	

	53,3	24,6	22,1											192	186	195	203
	52,9	25	22,1											75	71	81	90
	52,8	25,7	21,5											117	94	104	131
	52,7	26	21,3											161	143	151	173
	52,4	25,6	22											150	141	151	161
	52,3	27,4	20,3											125	118	130	135
	51,7	27,7	20,6											110	96	108	121
	51,5	26,8	21,7											120	101	107	127
	51,2	27,4	21,4											98	93	98	102
	51	28,7	20,3											106	93	103	112
	50,5	30,4	19,1											118	103	110	124
	47	33,1	19,9											53	50	56	58
(Santos <i>et al.</i> , 2008)	50,55	36,33							13,12					-55	-66	-49	-41
(Wu <i>et al.</i> , 2011)	37	50									10	3		-87	-120	-94	-61
(Turabi <i>et al.</i> , 2016)	42,1	48,7							9,2					-6	-16	-6	4
(Kainuma <i>et al.</i> , 1996)	50	50												674	660	707	719
	50	46						4						589	567	593	608
	50	42						8						473	459	485	503
	50	38						12						341	285	304	368
	50	34						16						191	128	134	192
	50	30						20						-22	-34	-12	-4
	44	46						10						268	259	348	362
	45	40						15						116	81	94	119
	55	30						15						386	378	433	449
(Zheng <i>et al.</i> , 2011)	49	39							12					-13	-34	1	22
(Koyama <i>et al.</i> , 2006)	50	36							14					-53	-63	-33	-23
(Aksoy <i>et al.</i> , 2009)	50,3	35,9								13,8				3	-8	2	17
	50,2	36,6								13,2				4	-3	7	18
	51,5	36								12,5				73	65	76	85
	50,3	39,6								10,1				171	95	107	184
	51,9	42,7								5,4				436	348	359	468
(Caputo and Solomon 2017)	49,5	27,8	22,7											36,9	17,1	33,9	57,6
(Mostafaei <i>et al.</i> , 2017)	49,6	30,8	19,6											36	31,5	42	46,5

3. CONCLUSION

Shape memory alloys are defined undeniably positioned in the technology. However, in terms of production costs, it is necessary to search for alloy types that will become an alternative to high-grade alloys such as NiTi and to present the service of humanity. From this point of view, successful studies with elements such as manganese, which can be provided as cheaper than the titanium element in nickel-based SHA, have been investigated. It has been found that in the determined thermal phase temperature transformations, the alloys' high nickel, manganese and gallium ratios are largely determinative. As a result of these studies, a wide range of transformation temperatures have been identified and found to be open to Research & Development. These types of alloys that provide the wide range of conversion can respond to many needs.

REFERENCES

- Aksoy, S., M. Acet, E. F. Wassermann, T. Krenke, X. Moya, L. Manosa, A. Planes and P. P. Deen (2009). "Structural properties and magnetic interactions in martensitic Ni-Mn-Sb alloys." *Philosophical Magazine*, Vol. 89, No. 22-24, pp. 2093-2109.
- Aldas, K., M. Eskil and İ. Özkul (2014). "Prediction of A f temperature for copper based shape memory alloys." *Indian Journal of Engineering & Materials Science* Vol. 21, pp. 429-437.
- Aldas, K. and I. Ozkul (2016). "Determination of the transformation temperatures of aged and low manganese rated Cu-Al-Mn shape memory alloys." *Journal of the balkan tribological association*, Vol. 22, No. 1, pp. 56-65.
- Babita, I., M. M. Raja, R. Gopalan, V. Chandrasekaran and S. Ram (2007). "Phase transformation and magnetic properties in Ni-Mn-Ga Heusler alloys." *Journal of alloys and compounds*, Vol. 432, No. 1, pp. 23-29.
- Buehler, W. J., J. Gilfrich and R. Wiley (1963). "Effect of low-temperature phase changes on the mechanical properties of alloys near composition TiNi." *Journal of applied physics*, Vol. 34, No. 5, pp. 1475-1477.
- Canbay, C. A. (2017). "Kinetic parameters and structural variations in Cu-Al-Mn and Cu-Al-Mn-Mg shape memory alloys." *AIP Conference Proceedings*, pp.120001.
- Canbay, C. A., S. Ozgen and Z. K. Genc (2014). "Thermal and microstructural investigation of Cu-Al-Mn-Mg shape memory alloys." *Applied Physics A*, Vol. 117, No. 2, pp. 767-771.
- Canbay, C. A. and İ. Özkul (2018). "Aging effects on transformation temperatures and enthalpies for TiNi alloy." *Turkish Journal of Engineering (TUJE)*, Vol. 2, No. 1, pp. 7-11.
- Canbay, C. A., A. Tekataş and İ. Özkul (2017). "Fabrication Of Cu-Al-Ni shape memory thin film by thermal evaporation." *Turkish Journal of Engineering (TUJE)*, Vol. 1, No. 2, pp. 27-32.
- Caputo, M. and C. Solomon (2017). "A facile method for producing porous parts with complex geometries from ferromagnetic Ni-Mn-Ga shape memory alloys." *Materials Letters*, Vol. 200, No., pp. 87-89.
- Duerig, T. and A. Pelton (1994). "Ti-Ni shape memory alloys." *Materials properties handbook: titanium alloys*, Vol., No., pp. 1035-1048.
- Eskil, M., K. Aldaş and İ. Özkul (2015). "Prediction of thermodynamic equilibrium temperature of Cu-based shape-memory smart materials." *Metallurgical and Materials Transactions A*, Vol. 46, No. 1, pp. 134-142.
- Glavatsky, I., N. Glavatska, O. Söderberg, S.-P. Hannula and J.-U. Hoffmann (2006). "Transformation temperatures and magnetoplasticity of Ni-Mn-Ga alloyed with Si, In, Co or Fe." *Scripta materialia*, Vol. 54, No. 11, pp. 1891-1895.
- Hodgson, D. E., W. Ming and R. J. Biermann (1990). "Shape memory alloys." *ASM International, Metals Handbook, Tenth Edition.*, Vol. 2, No., pp. 897-902.
- Huang, W. and W. Toh (2000). "Training two-way shape memory alloy by reheat treatment." *Journal of materials science letters*, Vol. 19, No. 17, pp. 1549-1550.
- Jiang, C., G. Feng, S. Gong and H. Xu (2003). "Effect of Ni excess on phase transformation temperatures of NiMnGa alloys." *Materials Science and Engineering: A*, Vol. 342, No. 1, pp. 231-235.
- Jiang, C., G. Feng and H. Xu (2002). "Co-occurrence of magnetic and structural transitions in the Heusler alloy Ni 53 Mn 25 Ga 22." *Applied physics letters*, Vol. 80, No. 9, pp. 1619-1621.
- Kainuma, R., K. Ishida and H. Nakano (1996). "Martensitic transformations in NiMnAl β phase alloys." *Metallurgical and Materials Transactions A*, Vol. 27, No. 12, pp. 4153-4162.
- Koho, K., O. Söderberg, N. Lanska, Y. Ge, X. Liu, L. Straka, J. Vimpari, O. Heczko and V. Lindroos (2004). "Effect of the chemical composition to martensitic transformation in Ni-Mn-Ga-Fe alloys." *Materials Science and Engineering: A*, Vol. 378, No. 1, pp. 384-388.
- Koyama, K., K. Watanabe, T. Kanomata, R. Kainuma, K. Oikawa and K. Ishida (2006). "Observation of field-induced reverse transformation in ferromagnetic shape memory alloy Ni 50 Mn 36 Sn 14." *Applied physics letters*, Vol. 88, No. 13, pp. 132505.
- Lanska, N., O. Söderberg, A. Sozinov, Y. Ge, K. Ullakko and V. Lindroos (2004). "Composition and temperature dependence of the crystal structure of Ni-Mn-Ga alloys." *Journal of Applied Physics*, Vol. 95, No. 12, pp. 8074-8078.

- Liu, Y. (2010). "Some factors affecting the transformation hysteresis in shape memory alloys." *Chen HR, editor*, Vol., No., pp. 361-369.
- Ma, J., I. Karaman and R. D. Noebe (2010). "High temperature shape memory alloys." *International Materials Reviews*, Vol. 55, No. 5, pp. 257-315.
- Mertmann, M. and G. Vergani (2008). "Design and application of shape memory actuators." *The European Physical Journal Special Topics*, Vol. 158, No. 1, pp. 221-230.
- Mihálcz, I. (2001). "Fundamental characteristics and design method for nickel-titanium shape memory alloy." *Periodica Polytechnica. Engineering. Mechanical Engineering*, Vol. 45, No. 1, pp. 75.
- Mostafaei, A., K. A. Kimes, E. L. Stevens, J. Toman, Y. L. Krimer, K. Ullakko and M. Chmielus (2017). "Microstructural evolution and magnetic properties of binder jet additive manufactured Ni-Mn-Ga magnetic shape memory alloy foam." *Acta Materialia*, Vol. 131, No., pp. 482-490.
- Ozkul, I., C. A. Canbay, F. Aladağ and K. Aldaş (2017). "The effect of the aging period on the martensitic transformation and kinetic characteristic of at% Cu68.09Al26.1Ni1.54Mn4.27 shape memory alloy." *Russian Journal of Non-Ferrous Metals*, Vol. 58, No. 2, pp. 130-135.
- Santos, J. D., T. Sanchez, P. Alvarez, M. Sanchez, J. L. Sánchez Llamazares, B. Hernando, L. Escoda, J. J. Suñol and R. Varga (2008). "Microstructure and magnetic properties of Ni 50 Mn 37 Sn 13 Heusler alloy ribbons." *Journal of Applied Physics*, Vol. 103, No. 7, pp. 07B326.
- Schroeder, T. and C. Wayman (1977). "The two-way shape memory effect and other "training" phenomena in Cu Zn single crystals." *Scripta metallurgica*, Vol. 11, No. 3, pp. 225-230.
- Sreekumar, M., T. Nagarajan and M. Singaperumal (2009). "Application of trained NiTi SMA actuators in a spatial compliant mechanism: Experimental investigations." *Materials & Design*, Vol. 30, No. 8, pp. 3020-3029.
- Stöckel, D. (1995). "The shape memory effect-phenomenon, alloys and applications." *California*, Vol. 94539, No., pp. 1-13.
- Sun, L., W. M. Huang, Z. Ding, Y. Zhao, C. C. Wang, H. Purnawali and C. Tang (2012). "Stimulus-responsive shape memory materials: a review." *Materials & Design*, Vol. 33, No., pp. 577-640.
- Turabi, A., P. Lázpita, M. Sasmaz, H. Karaca and V. Chernenko (2016). "Magnetic and conventional shape memory behavior of Mn–Ni–Sn and Mn–Ni–Sn (Fe) alloys." *Journal of Physics D: Applied Physics*, Vol. 49, No. 20, pp. 205002.
- Wu, S. and S. Yang (2003). "Effect of composition on transformation temperatures of Ni–Mn–Ga shape memory alloys." *Materials Letters*, Vol. 57, No. 26, pp. 4291-4296.
- Wu, Z., Z. Liu, H. Yang, Y. Liu and G. Wu (2011). "Metamagnetic phase transformation in Mn 50 Ni 37 In 10 Co 3 polycrystalline alloy." *Applied Physics Letters*, Vol. 98, No. 6, pp. 061904.
- Zheng, H., D. Wu, S. Xue, J. Frenzel, G. Eggeler and Q. Zhai (2011). "Martensitic transformation in rapidly solidified Heusler Ni 49 Mn 39 Sn 12 ribbons." *Acta Materialia*, Vol. 59, No. 14, pp. 5692-5699.

Copyright © Turkish Journal of Engineering (TUJE).
All rights reserved, including the making of copies
unless permission is obtained from the copyright
proprietors.

Turkish Journal of Engineering



Turkish Journal of Engineering (TUJE)
Vol. 2, Issue 3, pp. 107-112, September 2018
ISSN 2587-1366, Turkey
DOI: 10.31127/tuje.395259
Research Article

INVESTIGATION OF DISSOLUTION KINETICS OF Zn AND Mn FROM SPENT ZINC-CARBON BATTERIES IN SULPHURIC ACID SOLUTION

Tevfik Agacayak ^{*1} and Ali Aras ²

¹ Selçuk University, Engineering Faculty, Department of Mining Engineering, Konya, Turkey
ORCID ID 0000-0001-8120-8804
tevfik@selcuk.edu.tr

² Selçuk University, Engineering Faculty, Department of Mining Engineering, Konya, Turkey
ORCID ID 0000-0001-8111-6176
aliaras@selcuk.edu.tr

* Corresponding Author

Received: 15/02/2018 Accepted: 01/03/2018

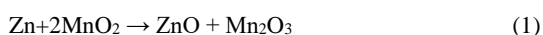
ABSTRACT

The aim of this study is to examine the dissolution kinetics of zinc and manganese from spent zinc-carbon battery in sulphuric acid solution. The leaching experiments were carried under the following conditions: leaching temperatures of 30°C, 40°C and 50°C; sulphuric acid concentration of 0.5 M; stirring speed of 400 rpm; solid/liquid ratio of 5/500 g/mL and particle size of -53 µm. In these conditions, while all of the zinc was dissolved, about 69 % of manganese was dissolved. To determine the kinetics of dissolution of the zinc and manganese in sulphuric acid medium, different shrinking core models were applied to the dissolution recoveries obtained at variable temperatures. Kinetics analysis showed that the zinc and manganese dissolution from spent zinc-carbon battery could be described by diffusion from product layer. The activation energies (E_a) and Arrhenius constants for the dissolution reactions were calculated. Activation energies (E_a) were determined for Zn and Mn as 94.53 kJ/mol and 1.41 kJ/mol, respectively.

Keywords: *Leaching, Dissolution kinetics, Zn-C battery, Zn, Mn, Activation energy, Sulphuric acid*

1. INTRODUCTION

Zinc-carbon type dry cell batteries are being commonly used during last 150 years in the world. There are two types of zinc carbon batteries mainly as leclanche battery and zinc chloride battery. A battery is an apparatus which converts the chemical energy into electric energy by an oxidation–reduction (redox) reaction. They are widely used in small household apparatus like flash light, toys, radios, watches, etc. In these batteries, anode material is zinc and the cathode is a mixture of manganese dioxide and carbon. Because of the spent zinc–carbon batteries contain zinc, manganese dioxide and also zinc oxide and manganese (III) oxide produced from discharging reaction (Bernardes, *et al.*, 2004; Park, *et al.*, 2006; Shin, *et al.*, 2009), they are important secondary source of Mn and Zn. During discharging, a chemical change occurs in the battery which can be expressed by the following reaction:



A lot of studies were found related with hydrometallurgical processes for recovery of manganese and zinc from spent zinc–carbon batteries in the literature (Shin, *et al.*, 2009; Ferella, *et al.*, 2008; Baba, *et al.*, 2009; sayilgan, *et al.*, 2010; Geęa and Walkowiak, 2011; Kursunoglu and Kaya, 2014; Buzatu, *et al.*, 2014; Taner, *et al.*, 2016; Abedin, *et al.*, 2017; Chen, *et al.*, 2017). Generally, these studies were carried out using only basic solution, acidic solution (hydrochloric acid, sulphuric acid) or reductive agents with these acid solutions. However, dissolution kinetics of manganese and zinc from spent zinc–carbon batteries were studied (Baba *et al.*, 2009; Geęa and Walkowiak, 2011; Taner, *et al.*, 2016).

Because, it is harmful to the environment discard of spent batteries is prohibited by stringent environmental regulations in most countries. In the event of the disposal or incineration of waste batteries, heavy metals may contaminate the environment. Therefore, it must be given to importance to collecting and recycling of spent batteries. Prevention of environmental pollution and research for the recycling of precious metals have become an important issue. For this reason, the application of hydrometallurgical processes has been carried out considering the economic and environmental suitability.

In this work, it is aimed to dissolution of manganese and zinc in sulphuric acid solution from spent zinc carbon batteries. In addition, the dissolution kinetics were

studied and the activation energies required for dissolution were calculated.

2. MATERIAL AND METHOD

In this study, spent zinc–carbon batteries were used which collected from Selçuk University spent battery boxes. The plastic, paper and metal parts were removed from the zinc-carbon batteries that were passed through processes such as separation, dismantling. The separated pieces of the spent zinc-carbon battery were weighed and the weight percentages were determined as 56.42% black paste, 13.84% steel can, 11.58% zinc can, 7.65% carbon rod, 4.65% paper, 3.33% plastic and 2.53% metal cover and bottom. The obtained black paste was dried at 105°C for 24 hours. Moisture of black paste was calculated as 12.51%. The battery powder was ground using a ball mill and sieved to obtain particle size less than 106 µm. The original powder was washed to remove electrolyte with distilled water in a glass vessel at 60°C and dried to remove external impurities at 105°C for 24 hours. Then the powder was burned for one hour at 600°C in the furnace, to remove paper, plastic and carbon residues. Sieving was carried out and -106+75, -75+53, -53 µm particle size fractions were obtained. Approximately, 2 grams of sample was weighed and dissolved in the king water (HNO₃ + 3HCl) in a Teflon vessel. The solutions were diluted with distilled water to 100 ml in a volumetric flask. The amount of Mn and Zn was measured using a GBC brand SensAA model flame atomic absorption spectrometer (AAS). The manganese-zinc contents of waste battery powder of the original (-106 µm), washed (-106 µm) and -53 µm particle size were given in Table 1.

Table 1. Zn–Mn content of spent zinc–carbon battery

Particle size, µm	Zn,%	Mn,%
Original (-106)	21.52	34.34
Washed (-106)	22.87	35.87
-53	20.11	36.46

The washed powders were analyzed by X-ray diffraction (XRD) to determine the mineralogical composition of powders and shown in Fig. 1. XRD analyses showed the presence of ZnO, MnO₂ and Mn₂O₃.

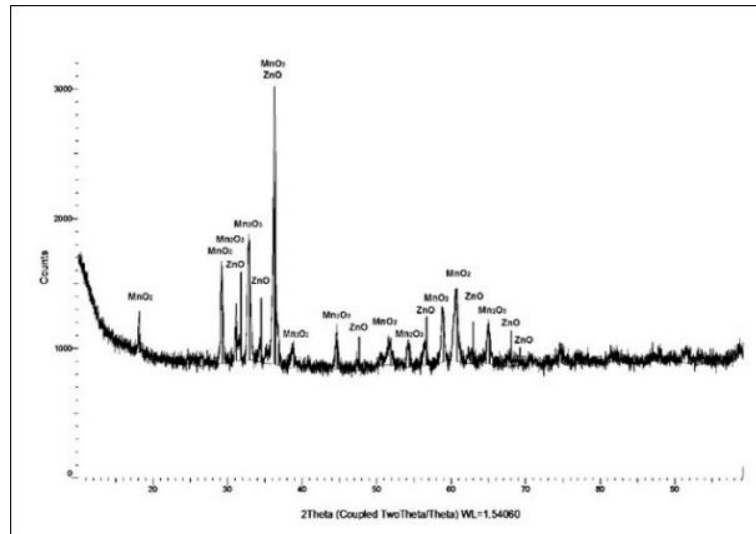


Fig. 1. XRD pattern of spent Zn-C battery powder.

Leaching experiments were carried out in a 1 L volume of glass vessel placed in a thermostatically-controlled water bath. The leach solution was stirred by Heidolph brand RZR 2021 model mechanical stirrer with teflon lined impeller. Schematic view of the experimental procedure is given in Fig. 2. 1 mL of leaching solution was gotten from the reactor at various time intervals and diluted with water to 100 mL in a volumetric flask. The dissolution amounts of Zn and Mn were determined by AAS.

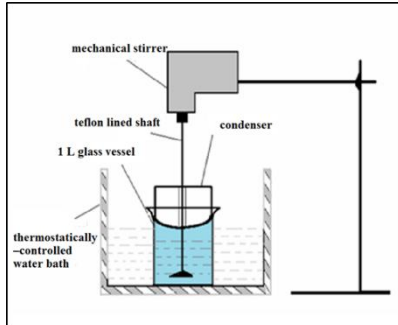


Fig. 2. Schematic view of the experimental procedure.

Table 2. Effect of temperature on Zn and Mn extraction.

Leaching Time (min)	Zn and Mn extraction (%)					
	30°C		40°C		50°C	
	Zn	Mn	Zn	Mn	Zn	Mn
5	65.01	29.79	78.91	49.21	96.84	58.03
10	65.79	32.94	80.32	53.11	97.43	61.02
15	67.06	33.80	82.36	55.06	98.49	62.11
30	68.02	39.01	90.94	58.16	100	64.02
45	69.03	45.02	92.66	59.03	100	66.03
60	71.35	50.67	95.66	62.72	100	68.46

3.2. Kinetic Models

Generally, the leaching process for heterogeneous reactions uses the shrinking core models controlling by chemical reaction, diffusion, and the diffusion through the product layer these kinetic models (Habashi, 1969;

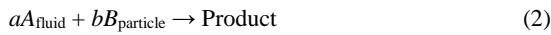
RESULTS AND DISCUSSION

3.1. Experimental Results

Leaching experiments were carried out using 500 mL solution of 0.5 mol/L sulphuric acid concentration. Battery powder in -53 μm fraction was used. 5 g of battery powder was used. Leaching solution was stirred at 400 rpm at 60 min of leaching time. Under these conditions, leaching experiments were performed at different temperatures (30°C, 40°C and 50°C). The results of these experiments, Zn and Mn extraction recoveries were given in Table 2. It can be seen from the Table 2 that Zn and Mn extraction recoveries increased with increasing temperature and leaching time. In these conditions, while all of the zinc was dissolved, about 69% of manganese was dissolved. The reason of this, since the leaching rate of manganese was increasing slightly in sulfuric acid leaching experiment, due to the insoluble of Mn^{4+} . The reduction potential needs to be modified to turn Mn^{4+} into Mn^{2+} (Takeno, 2005).

Levenspiel, 1999; Sohn and Wadsworth, 1986). This model was chosen because it is the most suitable model for dissolution reactions.

The dissolution of Zn and Mn from spent zinc-carbon battery can be explained by a shrinking core model which can be expressed as follows:



To describe the dissolution of Zn and Mn from battery powder, a kinetic investigation was applied to results in Table 2. In shrinking core model, if the reaction is controlled by surface reaction,

$$1 - (1 - x)^{1/3} = k_s t \quad (3)$$

if the reaction is controlled by film diffusion,

$$1 - (1 - x)^{2/3} = k_f t \quad (4)$$

if the reaction is controlled by diffusion from product layer

$$1 - \frac{2}{3}x - (1 - x)^{2/3} = k_d t \quad (5)$$

equations were used, where x is the fraction reacted, t is the reaction time (min), k_s , k_f and k_d are the rate constants (Levenspiel, 1999; Habashi, 1969). Eqs. (3,5) were applied to the experimental results. The correlation coefficients and apparent rate constants for each temperature were given in Table 3.

Considering the values given in Table 3, manganese and zinc dissolution from spent zinc-carbon battery could be described by the diffusion from product layer. Plots of $1-2/3x-(1-x)^{2/3}$ for various temperatures of Zn and Mn were given in Fig. 3 and Fig. 4.

Table 3. Values of k_s , k_f , k_d and correlation coefficients for variable temperatures.

Temperature, °C	Surface Reaction $1-(1-x)^{1/3}$		Film Diffusion $1-(1-x)^{2/3}$		Diffusion from Product Layer $1-2/3x-(1-x)^{2/3}$	
	Apparent rate constant (k_s) $\times 10^{-3}$ for Zn	Correlation coefficient, (R ²)	Apparent rate constant (k_f) $\times 10^{-3}$ for Zn	Correlation coefficient, (R ²)	Apparent rate constant (k_d) $\times 10^{-3}$ for Zn	Correlation coefficient, (R ²)
30	0.74921	0.97	1.02212	0.96	0.97406	0.97
40	4.58120	0.97	4.37922	0.96	6.74515	0.97
50	6.57444	0.96	4.09939	0.99	9.75871	0.99
Temperature, °C	Surface Reaction $1-(1-x)^{1/3}$		Film Diffusion $1-(1-x)^{2/3}$		Diffusion from Product Layer $1-2/3x-(1-x)^{2/3}$	
	Apparent rate constant (k_s) $\times 10^{-3}$ for Mn	Correlation coefficient, (R ²)	Apparent rate constant (k_f) $\times 10^{-3}$ for Mn	Correlation coefficient, (R ²)	Apparent rate constant (k_d) $\times 10^{-3}$ for Mn	Correlation coefficient, (R ²)
30	1.74282	0.99	2.92762	0.99	1.39855	0.99
40	1.22527	0.96	1.85357	0.96	1.35096	0.97
50	1.09626	0.96	1.56221	0.95	1.36704	0.97

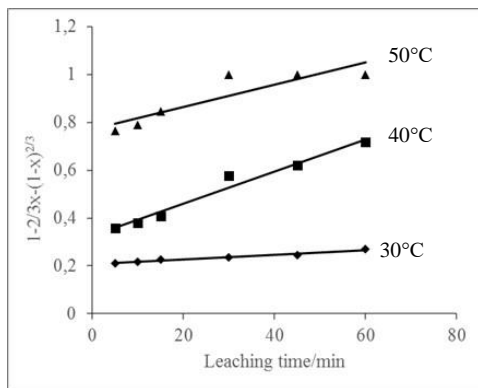


Fig. 3. The variation in $1-2/3x-(1-x)^{2/3}$ with time at various temperatures for Zn.

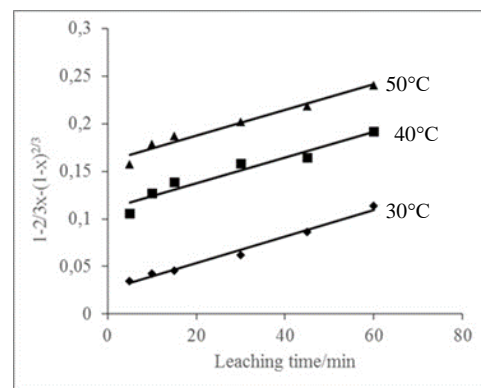


Fig. 4. The variation in $1-2/3x-(1-x)^{2/3}$ with time at various temperatures for Mn.

3.3. Determination of Activation Energy

Apparent rate constants (k) at different temperatures were obtained from the slope of the linear plots in Fig. 3 and Fig. 4 for zinc and manganese respectively. Then the values of reaction rate constants (k) were plotted according to the Arrhenius type equation. The plot of $\ln k_d$ vs. $1000/T(K^{-1})$ was straight line for both zinc and manganese. The Arrhenius graphics were plotted using the apparent rate constants obtained by application of Eq. (5) (Figs. 5,6). The activation energies required for dissolution of Zn and Mn were calculated as to be 94.53 kJ/mol and 1.41 kJ/mol, respectively. Similarly, in some kinetic studies using various acid media related with zinc and manganese dissolution from spent zinc-carbon batteries, shrinking core model was used. In these studies, activation energies were given as 22.78 kJ/mol, 23.03 kJ/mol for Zn (Baba, *et al.*, 2009; Taner, *et al.*, 2016) and 7.04 kJ/mol, 31.80 kJ/mol for Mn, respectively (Kursunoglu and Kaya, 2014; Taner, *et al.*, 2016).

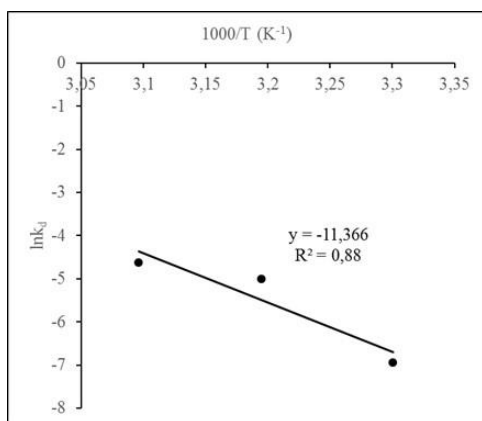


Fig. 5. Arrhenius plot of reaction rate against reciprocal temperature for dissolution of Zn.

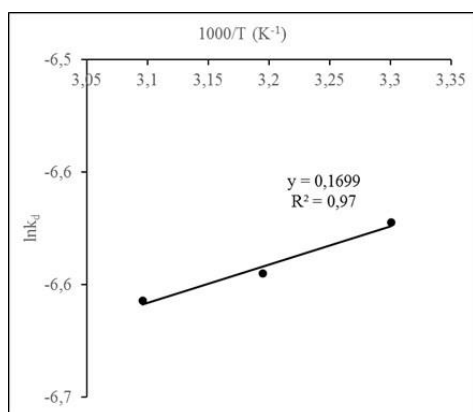


Fig. 6 Arrhenius plot of reaction rate against reciprocal temperature for dissolution of Mn.

4. CONCLUSION

Dissolution kinetics of zinc and manganese from spent zinc-carbon batteries in sulphuric acid solution was investigated. Therefore, leaching experiments were performed using some constant parameters (sulphuric

acid concentration of 0.5 M; stirring speed of 400 rpm; solid/liquid ratio of 5/500 g/mL and particle size of -53 μm) at different temperatures (30°C, 40°C and 50°C). It was found that the dissolution rate increased with increase in the leaching temperature and leaching time. At 30°C, dissolution of Mn and Zn was reached at 60 min 50.67% and 71.35%, respectively. At 50°C, the best dissolutions of Mn and Zn were obtained as to be 68.46% and 100%.

In order to determine the dissolution kinetics of Zn and Mn, shrinking core model was applied to dissolution recoveries obtained at different temperatures. It was determined that zinc and manganese dissolved in sulphuric acid solution from spent zinc-carbon batteries by diffusion from product layer. Activation energies (E_a) were calculated for Zn and Mn as 94.53 kJ/mol and 1.41 kJ/mol, respectively.

REFERENCES

- Abedin, M. R., Abedin, S., Mahbub, H. A., Nandini, D., Khan, M. S. (2017). "A Hydrometallurgical Approach to Recover Zinc and Manganese from Spent Zn-C Batteries", *Materials Science Forum*, Vol. 886, pp. 117-121.
- Baba, A. A., Adekola, A. F., Bale, R. B. (2009). "Development of a combined pyro- and hydro-metallurgical route to treat spent zinc-carbon batteries. *Journal of Hazardous Mat.*, Vol. 171, pp. 838-844.
- Bernardes, A. M., Espinosa, D. C. R., Tenorio J. A. S. (2004). "Recycling of batteries: a review of current processes and Technologies" *Journal of Power Sources*, Vol. 130, pp.291-298.
- Buzatu, M., Saceanu, S., Petrescu, M. I., Ghica, G. V., Buzatu, T. (2014). "Recovery of zinc and manganese from spent batteries by reductive leaching in acidic media" *Journal of Power Sources*, Vol. 247, pp. 612-617.
- Chen, W. S., Chin, T.L., Kuan, Y. L. (2017). "Recovery Zinc and Manganese from Spent Battery Powder by Hydrometallurgical Route" *Energy Procedia*, Vol. 107, pp. 167-174.
- Ferella, F., DeMichelis, I., Veglio, F. (2008). "Process for the recycling of alkaline and zinc-carbon spent batteries" *Journal of Power Sources*, Vol.183, 805-811.
- Gęga, J., Walkowiak, W. (2011). "Leaching of zinc and manganese from used up zinc-carbon batteries using aqueous sulfuric acid solutions" *Physicochem. Probl. Miner. Process.*, Vol. 46, pp. 155-162.
- Habashi, F. (1969). *Principles of extractive metallurgy* New York: Gordon and Breach.
- Kursunoglu, S, Kaya, M. (2014). "Dissolution and precipitation of zinc and manganese obtained from spent zinc-carbon and alkaline battery powder" *Physicochem. Prob. Miner. Process.*, Vol. 50, No.1, pp. 41-55.
- Levenspiel, O. (1999). *Chemical reaction engineering*, New York: John Wiley & Sons.

Park, J., Kang, J., Sohn, J., Yang, D., Shin, S. (2006). "Physical treatment for recycling commercialization of spent household batteries" *J. Korean Inst. Resour. Recycl.*, Vol:15 No:6, pp. 48–55.

Sayilgan, E., Kukrer, T., Yigit, N. O., Civelekoglu, G., Kitis, M. (2010). "Acidic leaching and precipitation of zinc and manganese from spent battery powders using various reductants" *J. Hazard. Mater.*, Vol. 173, pp.137–143.

Shin, S., Senanayake, G., Sohn J., Park, J., Kang, J., Yang D., Kim T. (2009). "Separation of zinc from spent zinc–carbon batteries by selective leaching with sodium hydroxide", *Hydrometallurgy*, Vol. 96, pp. 349–353.

Sohn, H. Y., Wadsworth, M. E. (1986). *Cr'nética de los procesos de la Metalurgia Extractiva* (translated from English Version). Ed. Trillas, Mexico. Takeno, N., (2005) "Atlas of Eh-pH diagrams Intercomparison of thermodynamic databases", National Institute of Advanced Industrial Science and Technology, Japan.

Taner, H. A., Aras, A., Agacayak, T. (2016). "Determination of dissolution kinetics of manganese and zinc from spent zinc–carbon batteries in acidic media" 1. *International Academic Research Congress*, Ines 2016, Anyalya/Side/ Turkey, pp. 379-383.

Copyright © Turkish Journal of Engineering (TUJE).
All rights reserved, including the making of copies
unless permission is obtained from the copyright
proprietors.

Turkish Journal of Engineering



Turkish Journal of Engineering (TUJE)
Vol. 2, Issue 3, pp. 113-118, September 2018
ISSN 2587-1366, Turkey
DOI: 10.31127/tuje.385008
Research Article

COMPARATIVE STUDY OF REGIONAL CRASH DATA IN TURKEY

Murat Ozen *¹

Mersin University, Engineering Faculty, Department of Civil Engineering, Mersin, Turkey
ORCID ID 0000-0002-1745-7483
ozen.murat@mersin.edu.tr

* Corresponding Author

Received: 28/01/2018

Accepted: 10/04/2018

ABSTRACT

This study provides a comparative analysis of traffic safety in Turkey across the seven geographic regions over a 11 year time frame (2006 to 2016). The comparisons are performed in relative terms and absolute terms. Fatal and/or injury (FI) crashes per million population and per million registered vehicles were used to quantify safety. For the ordinal analysis, rates for the regions were ranked individually for each year as well as for the 11 years aggregated. An examination of the results indicated that the relative ranks of the regions were stable over the study period. Depending on the safety measure used, the relative rankings of regions varied. It means that a region ranked at the top (high crash rate) for one safety measure does not need to be ranked again at the top for other safety measure. For the cardinal analysis, the computed rates were used. These results were consistent with those from the ordinal analysis, but showed greater variability in the rates over time, which means that FI crash rates significantly increased over the time. A Geographic Information Systems based thematic maps were used to support these efforts.

Keywords: *Comparative Safety Analysis, Crash Rates, Data Visualization, Traffic Safety*

1. INTRODUCTION

Even though there has been significant public policy attention and improvements in traffic safety policies and practices in Turkey, 61 people died per billion vehicle-km in traffic crashes in 2016 (TGDH, 2017; TurkStat, 2018a). In spite of significant improvements in national highway network, there has been an increase in fatal and/or injury (FI) crashes over the last decade (TurkStat, 2018a). The distribution of crashes across the nation is also of importance to transportation system owners. National and local safety programs aim to reduce crashes and the severity of their outcomes within their jurisdictions. Development of geographically appropriate safety strategies requires estimating pertinent crash and exposure data at the relevant spatial scale. While data required to identify safety risks are collected at the local level, published databases are typically available only at larger scales. Thus, there is a need to deduce data at the local level (i.e., lower levels of spatial aggregation) from partially complete or surrogate datasets that are available at a higher level of aggregation.

FI crashes are reported by the traffic police and gendarmerie units according to their areas of responsibility in Turkey. Disaggregate statistics of these crashes are published annually by Turkish Statistical Institute (TurkStat). This aggregate database provides temporal and provincial distribution of the crashes as well as type of vehicles involved, classification of the crash locations as well as gender and age distribution of the crash victims. Due to the lack of disaggregate crash level data at the national level, province and regional variations of traffic safety have not been examined in detail. Recently, Atalay and Tortum (2015) compared the number of fatalities per traffic crashes and per kilometer of road network across the 81 provinces of Turkey. The results showed that number of fatalities per crash are higher in less developed provinces, whereas number of fatalities per length of road network are higher in developed provinces. In other study, Erdogan (2009) studied the provincial level differences in number of FI crashes and number of fatalities. Population and number of registered vehicles were used to quantify safety and results indicated that provinces with higher FI crashes and fatalities were located in the provinces that contain the roads connecting the İstanbul, Ankara, and Antalya provinces. However, there is no study focusing on traffic safety at the regional level in Turkey.

This study provides a comparative analysis of the FI crashes across the seven geographic regions in Turkey from 2006 to 2016 (additional information is provided in Appendix A). The comparisons are performed in relative terms and absolute terms. Since vehicle-km data are not available either province or regional level, number of FI crashes per million population and per million registered vehicles are used to quantify safety. The principal sources of data used in this study is TurkStat.

2. METHODOLOGY

Number of FI crashes per million population and per million registered vehicles were determined for each geographic region annually for the study period. A Geographic Information Systems based thematic maps were used to support these efforts.

Traditional statistical tests based on the normality

assumption of the data. Since FI crash rates do not follow normal distribution either across the regions or over the years, nonparametric methods need to be used to study FI crash rates. An appropriate test to use for this purpose is the Kruskal-Wallis nonparametric test. In this study, hypotheses of the Kruskal-Wallis H test was that:

H₀: FI crash rates are the same for each region from 2006 to 2016

H₁: FI crash rates are not the same for each region from 2006 to 2016.

Based on the Kruskal-Wallis test, the null hypothesis, H₀, is to be rejected at the (100- α) percent level of confidence if the test statistic, H, falls in the critical region $H > \chi^2_{\alpha}$ with $v = (k-1)$ degrees of freedom. To control the familywise type I error in Kruskal-Wallis H test; the probability of rejecting at least one pair hypothesis given all pairwise hypotheses are true, adjusted p-values are calculated and used to make the decision for each pair. The following equations was used to calculate adjusted p-values for each of pairwise hypothesis. If the adjusted p-value is bigger than 1, it is set to 1.

$$p_{adj} = pK(K - 1)/2 \quad (1)$$

where; K = number of pairwise hypothesis, and p = significance level of pairwise hypothesis.

3. RESULTS

FI crash rates were calculated annually for each geographic region based on per million population and per million registered vehicles. The results are presented thematically in Tables B1 to B2 (see Appendix). It is noted that the numbers of the regions are given randomly. In these tables, a graded color pattern is used to indicate FI crash rates. The color gradation ranges from red to yellow or green. Dark red is used to indicate the higher FI crash rates and worse safety records, and dark green is used to indicate lower FI crash rates and best safety records. Lighter red, yellow and lighter green colors are used to achieve gradation.

Table B1 presents FI crash rates of each region per million population for each year during the study period. Table B2 presents FI crash rates of each region per million registered vehicles for each year during the study period. In addition, the average FI crash rates for each measure for the entire 11 year period as a whole are given in these tables. It is seen that FI crash rates for regions significantly increased for each measure from 2006 to 2016. Furthermore, Table B1 and B2 clearly indicate the stability of the relative FI crash rates of regions across the years. They show that regions that tended to have lower FI crash rates, had lower crash rates across the years; and, regions that tended to have higher FI crash rates, had higher crash rates across the years.

Kruskal-Wallis pairwise comparisons implied that FI crash rates per million population are not the same across the regions from 2006 to 2016 (i.e. $H = 31.50 > \chi^2_{0.05,9} = 12.59$). Fig. 1 and 2 present box plot and 95% confidence interval of FI crash rates of regions per million population. It is seen that FI crash rates in Central Anatolia Region (Region 5), Mediterranean Region (Region 4) and Aegean Region (Region 2) seems

relatively higher than the others. FI crash rates in Southeastern Anatolia Region (Region 3) and Eastern Anatolia Region (Region 6) seems relatively lower than the others.

Fig. 3 presents graphical Kruskal-Wallis multiple pairwise comparisons. The number below each region represents the average rank of regional FI crash rates over the 11 years period. Fig. 4 provides Kruskal-Wallis tests results for significant pairwise comparisons. However, most of them are not significant based on adjusted p-value (see Fig. 3). In Fig. 3, yellow lines represent the significant pairwise comparisons based on adjusted p-values. FI crash rates per million population for Central Anatolia Region (Region 5) and Aegean Region (Region 2) are significantly higher than Southeastern Anatolia Region (Region 3) and Eastern Anatolia Region (Region 6); for Mediterranean Region (Region 4) is significantly higher than Southeastern Anatolia Region (Region 3).

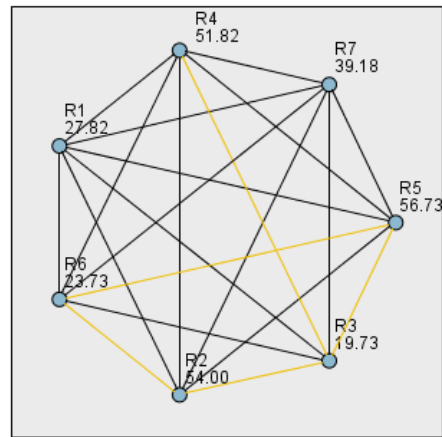


Fig. 3. Kruskal-Wallis multiple pairwise comparisons of FI crash rates per million population

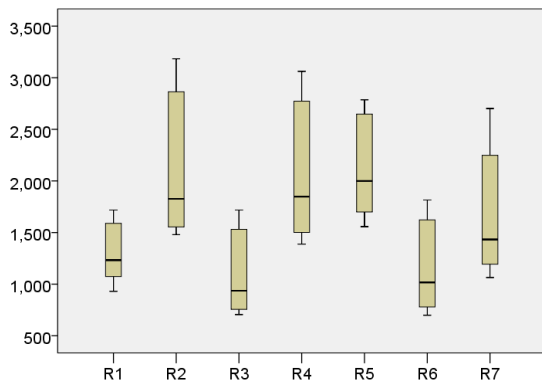


Fig. 1. Box plot of FI crash rates for regions per million population

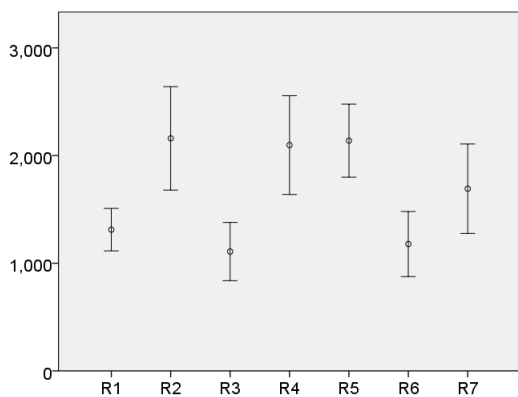


Fig. 2. 95% CI of mean FI crash rates for regions per million population

Sample1-Sample2	Test Statistic	Std. Error	Std. Test Statistic	Sig.	Adj.Sig.
R3-R5	-37.000	9.539	-3.879	.000	.002
R3-R2	34.273	9.539	3.593	.000	.007
R6-R5	33.000	9.539	3.459	.001	.011
R3-R4	-32.091	9.539	-3.364	.001	.016
R6-R2	30.273	9.539	3.173	.002	.032
R1-R5	-28.909	9.539	-3.030	.002	.051
R6-R4	28.091	9.539	2.945	.003	.068
R1-R2	-26.182	9.539	-2.745	.006	.127
R1-R4	-24.000	9.539	-2.516	.012	.249
R3-R7	-19.455	9.539	-2.039	.041	.870
R7-R2	14.818	9.539	1.553	.120	1.000
R6-R1	4.091	9.539	.429	.668	1.000
R7-R4	12.636	9.539	1.325	.185	1.000
R4-R2	2.182	9.539	.229	.819	1.000
R7-R5	17.545	9.539	1.839	.066	1.000
R3-R1	8.091	9.539	.848	.396	1.000
R4-R5	-4.909	9.539	-.515	.607	1.000
R6-R7	-15.455	9.539	-1.620	.105	1.000
R2-R5	-2.727	9.539	-.286	.775	1.000
R3-R6	-4.000	9.539	-.419	.675	1.000
R1-R7	-11.364	9.539	-1.191	.234	1.000

Fig. 4. Kruskal-Wallis multiple pairwise comparisons of FI crash rates per million population

Kruskal-Wallis pairwise comparisons implied that FI crash rates per million population are not the same across the regions from 2006 to 2016 (i.e. $H = 44.98 > \chi^2_{0.05,9} = 16.92$). Fig. 5 and 6 present box plot and 95% confidence interval of FI crash rates of regions per million population. It is seen that FI crash rates in Eastern Anatolia Region (Region 6) seems relatively higher than the others. FI crash rates in Marmara Region (Region 1) seems relatively lower than the others. Fig. 7 presents graphical Kruskal-Wallis multiple pairwise comparisons. Furthermore, Fig. 8 provides Kruskal-Wallis tests results for significant pairwise comparisons. However, most of them are not significant based on adjusted p-value. FI crash rates per million registered vehicles for Eastern Anatolia Region (Region 6) are significantly higher than Marmara Region (Region 1), Eagan Region (Region 2) and Mediterranean Region (Region 4). In addition, FI crash rates per million registered vehicles for Marmara Region (Region 1) are significantly lower than Southeastern Anatolia Region (Region 3), Central Anatolia Region (Region 5) and Black Sea Region (Region 7).

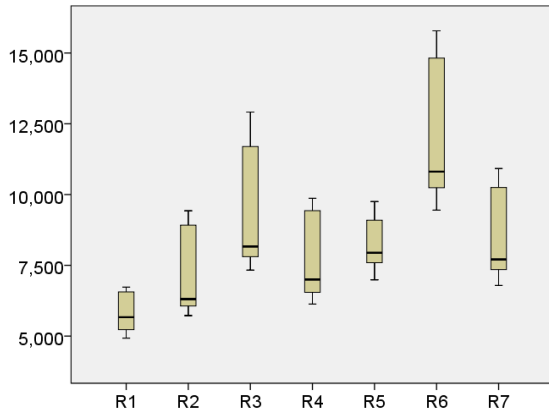


Fig. 5. Box plot of FI crash rates for regions per million registered vehicles

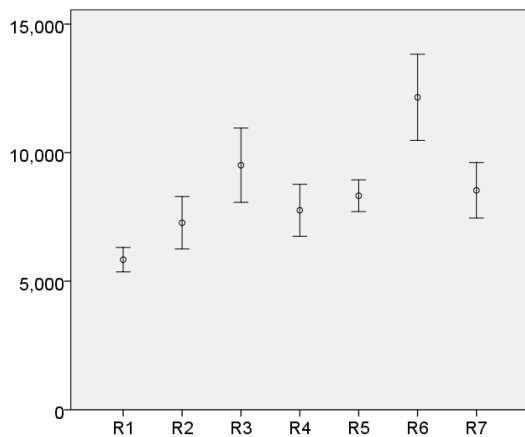


Fig. 6. 95% CI of mean FI crash rates for regions per million population.

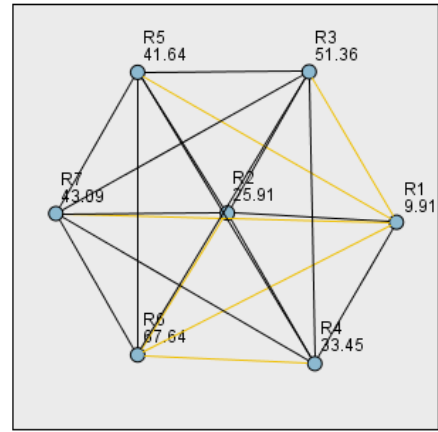


Fig. 7. Kruskal-Wallis multiple pairwise comparisons of FI crash rates per million registered vehicles

Sample1-Sample2	Test Statistic	Std. Error	Std. Test Statistic	Sig.	Adj.Sig.
R1-R3	-41.455	9.539	-4.346	.000	.000
R2-R6	-41.727	9.539	-4.374	.000	.000
R1-R6	-57.727	9.539	-6.051	.000	.000
R4-R6	-34.182	9.539	-3.583	.000	.007
R1-R7	-33.182	9.539	-3.478	.001	.011
R1-R5	-31.727	9.539	-3.326	.001	.019
R5-R6	-26.000	9.539	-2.726	.006	.135
R2-R3	-25.455	9.539	-2.668	.008	.160
R7-R6	24.545	9.539	2.573	.010	.212
R1-R4	-23.545	9.539	-2.468	.014	.285
R7-R3	8.273	9.539	.867	.386	1.000
R5-R3	9.727	9.539	1.020	.308	1.000
R4-R3	17.909	9.539	1.877	.060	1.000
R1-R2	-16.000	9.539	-1.677	.093	1.000
R4-R5	-8.182	9.539	-.858	.391	1.000
R5-R7	-1.455	9.539	-.152	.879	1.000
R2-R4	-7.545	9.539	-.791	.429	1.000
R3-R6	-16.273	9.539	-1.706	.088	1.000
R2-R5	-15.727	9.539	-1.649	.099	1.000
R4-R7	-9.636	9.539	-1.010	.312	1.000
R2-R7	-17.182	9.539	-1.801	.072	1.000

Fig. 8. Kruskal-Wallis multiple pairwise comparisons of FI crash rates per million population

Fig. 9 and 10 provide thematic maps based on the average ranks of the provinces for each of the safety measures used in this study. In these maps, the red colored provinces have the highest rates while the green colored provinces have the lowest rates. An examination for Fig. 1 to 2 reveal some interesting patterns in the spatial distribution of the relative safety ranks of the regions. Overall, it can be seen that Marmara Region (Region 1) tend to have best safety records. Relative safety records of Aegean Region (Region 2), Eastern Anatolia Region (Region 6) and Southeastern Anatolia Region (Region 3) are significantly different for million population and million registered vehicles measures. For instance, Eastern Anatolia Region (Region 6) has the best safety records for FI crash rates per million population, however, it has the worst safety records for FI crash rates per million registered vehicles.

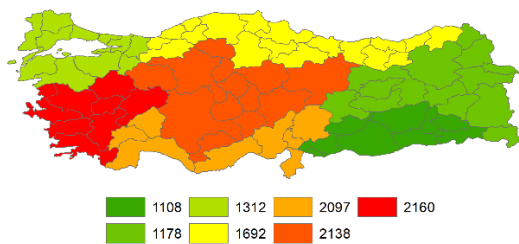


Fig 9. Average FI crash rates per million population for regions from 2006 to 2016

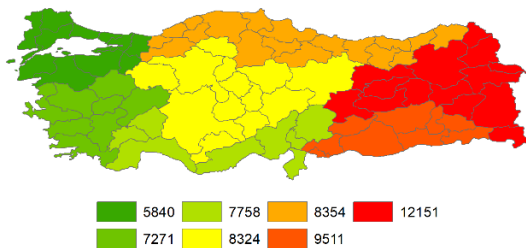


Fig. 10. Average FI crash rates per million registered vehicle for regions from 2006 to 2016

4. CONCLUSION

This paper summarized efforts of and findings from a study to examine regional level FI crash trends and perform comparative analyses of safety records 2006 to 2016. The comparisons were performed in relative terms (ordinal scale or based on rates) and absolute terms (cardinal or rank ordered scale). Two safety measures were used to evaluate safety: million population and million registered vehicles. Data were obtained from publications maintained by TurkStat.

An examination of the results indicated that the relative ranks of the regions were stable over the study period for each safety measure. Non-parametric statistical tests and thematic maps used to support comparative analyses. Specifically, the Kruskal-Wallis nonparametric test was used in this study. The results showed that the FI crash rates are not the same across the regions. Furthermore, the analyses also revealed that depending on the safety measure used, the relative rankings of regions

varied (i.e., a region ranked at the top (high crash rate) for one safety measure does not need to be ranked again at the top for other safety measure). This figure is resulted from significantly different vehicle ownership rate across the regions in Turkey. For the cardinal analysis the computed rates were used. These results were consistent with those from the ordinal analysis, but it was showed that FI crash rates significantly increased over the time.

For broad macro level analyses a more representative vehicle-km measure is required to study relative safety records of regions. However, it is available only for national level in Turkey. Furthermore, if specific analyses are required, then safety measures should be defined based on the desired evaluations. For example, if the goal were to address rural safety, the measures should be computed using rural fatal and/or injury crashes, rural vehicle-km, and the extent of rural kilometers of road network. This paper explored methods to analyze regional differences in road traffic safety. The results document the validity and promise of the methods. These methods could be expanded for policy and operational analyses.

REFERENCES

Erdogan, S. (2009). "Explorative spatial analysis of traffic accident statistics and road mortality among the provinces of Turkey". *Journal of safety research*, Vol. 40, No. 5, 341-351.

OECD/ITF. (2016). Organisation for Economic Co-operation and Development/International Transport Forum. *Road Safety Annual Report 2016*, Paris. OECD Publishing, 2016.

TGDH, Turkish General Directorate of Highways. (2017). *Karayolları Üzerindeki Seyir ve Taşımalar*. Turkey.

<http://www.kgm.gov.tr/SiteCollectionDocuments/KGMdocuments/Istatistikler/SeyirveTasimalar/SeyirVeTasimalar.pdf> [Accessed 10 Dec 2017].

Tortum, A. and Atalay, A. (2015). "Spatial analysis of road mortality rates in Turkey." In *Proceedings of the Institution of Civil Engineers-Transport*, Vol. 168, No. 6, pp. 532-542.

TurkStat, Turkish Statistical Institute. (2018a). *Road Traffic Accident Statistics*, 2015.

<http://www.turkstat.gov.tr/PreHaberBultenleri.do?id=21611> [Accessed 10 Dec 2017].

TurkStat, Turkish Statistical Institute. (2018b). *Road Traffic Accident Statistics*, 2016.

<http://www.turkstat.gov.tr/PreHaberBultenleri.do?id=24606> [Accessed 10 Dec 2017].

Copyright © Turkish Journal of Engineering (TUJE). All rights reserved, including the making of copies unless permission is obtained from the copyright proprietors.

Appendix A: Geographic Regions in Turkey

It is noted that the numbers of the regions are given randomly.

- Marmara Region (Region 1): Balıkesir, Bilecik, Bursa, Çanakkale, Edirne, İstanbul, Kırklareli, Kocaeli, Sakarya, Tekirdağ, Yalova.
- Aegean Region (Region 2): Afyon, Aydın, Denizli, İzmir, Kütahya, Manisa, Muğla, Uşak.
- Southeastern Anatolia Region (Region 3): Adıyaman, Batman, Diyarbakır, Gaziantep, Kilis, Mardin, Siirt, Urfa, Şırnak.
- Mediterranean Region (Region 4): Adana, Antalya, Burdur, Hatay, Isparta, Kahramanmaraş, Mersin, Osmaniye.
- Central Anatolia Region (Region 5): Aksaray, Ankara, Çankırı, Eskişehir, Karaman, Kayseri, Kırıkkale, Kırşehir, Konya, Nevşehir, Niğde, Sivas, Yozgat.
- Eastern Anatolia Region (Region 6): Ağrı, Ardahan, Bingöl, Bitlis, Elazığ, Erzincan, Erzurum, Hakkari, Iğdır, Kars, Malatya, Muş, Tunceli, Van.
- Black Sea Region (Region 7): Amasya, Artvin, Bartın, Bayburt, Bolu, Çorum, Düzce, Giresun, Gümüşhane, Karabük, Kastamonu, Ordu, Rize, Samsun, Sinop, Tokat, Trabzon, Zonguldak



Fig. A1. Geographical regions in Turkey

Appendix B: FI Crash Rates

Table B1. FI crash rates for regions per million population

Region	2006	2007	2008	2009	2010	2011	2012	2013	2014	2015	2016	Average 2006-2016
Marmara (R1)	930	1061	1051	1087	1091	1233	1376	1557	1621	1707	1718	1312
Aegean (R2)	1479	1564	1489	1544	1597	1826	2197	2766	2961	3183	3150	2160
Southeastern Anatolia (R3)	707	717	706	794	834	936	1153	1538	1564	1718	1524	1108
Mediterranean (R4)	1388	1481	1432	1522	1608	1848	2164	2749	2796	3061	3020	2097
Central Anatolia (R5)	1565	1678	1558	1720	1803	2000	2371	2675	2621	2745	2786	2138
Eastern Anatolia (R6)	699	749	726	808	942	1017	1159	1558	1688	1815	1797	1178
Black Sea (R7)	1065	1181	1093	1207	1304	1433	1608	2192	2304	2529	2702	1692

Table B2. FI crash rates for regions per million registered vehicle

Region	2006	2007	2008	2009	2010	2011	2012	2013	2014	2015	2016	Average 2006-2016
Marmara (R1)	4927	5378	5141	5265	5191	5669	6098	6666	6715	6731	6456	5840
Aegean (R2)	6276	6278	5725	5846	5852	6305	7263	8859	9175	9428	8979	7271
Southeastern Anatolia (R3)	8163	7839	7329	7771	7616	8077	9414	12098	12058	12916	11335	9511
Mediterranean (R4)	6626	6673	6130	6346	6469	6997	7802	9571	9403	9867	9459	7758
Central Anatolia (R5)	7636	7826	6986	7502	7551	7943	8989	9754	9214	9202	8963	8324
Eastern Anatolia (R6)	10189	10294	9449	9871	10621	10811	11614	14783	15399	15784	14859	12152
Black Sea (R7)	7384	7710	6788	7189	7313	7483	7935	10243	10255	10651	10920	8534

Turkish Journal of Engineering



Turkish Journal of Engineering (TUJE)
Vol. 2, Issue 3, pp. 119-124, September 2018
ISSN 2587-1366, Turkey
DOI: 10.31127/tuje.408976
Research Article

PERFORMANCE COMPARISON OF ANFIS, ANN, SVR, CART AND MLR TECHNIQUES FOR GEOMETRY OPTIMIZATION OF CARBON NANOTUBES USING CASTEP

Mehmet Acı¹, Çiğdem İnan Acı^{*2} and Mutlu Avcı³

¹ Mersin University, Faculty of Engineering, Department of Computer Engineering, Mersin, Turkey
ORCID ID 0000-0002-7245-8673
maci@mersin.edu.tr

² Mersin University, Faculty of Engineering, Department of Computer Engineering, Mersin, Turkey
ORCID ID 0000-0002-0028-9890
caci@mersin.edu.tr

³ Çukurova University, Faculty of Engineering, Department of Biomedical Engineering, Adana, Turkey
ORCID ID 0000-0002-4412-4764
mavci@cu.edu.tr

* Corresponding Author

Received: 22/03/2018

Accepted: 10/04/2018

ABSTRACT

Density Functional Theory (DFT) calculations used in the Carbon Nanotubes (CNT) design take a very long time even in the simulation environment as it is well known in literature. In this study, calculation time of DFT for geometry optimization of CNT is reduced from days to minutes using seven artificial intelligence-based and one statistical-based methods and the results are compared. The best results are achieved from ANFIS and ANN based models and these models can be used instead of CNT simulation software with high accuracy.

Keywords: *Geometry Optimization, Cnt, Dft, Artificial Intelligence*

1. INTRODUCTION

Density functional theory (DFT) (Kohn and Sham, 1965) is the most successful method that calculates atomic coordinates faster than other mathematical approaches and it also reaches more accurate results. DFT uses ground state energy formula which is developed by Kohn and Sham (Eq. (1)).

$$E = \sum_i^v \epsilon_j - \frac{1}{2} \int \frac{n(r)n(r')}{|r-r'|} dr dr' - \int v_{xc}(r)n(r)dr + E_{xc}[n(r)] \quad (1)$$

where the ϵ_j and n are the self-consistent quantities, V_{xc} is the exchange correlation potential energy, E_{xc} is the exchange correlation energy, and $n(r)$ is the electron density. However, the elapsed time for calculation of high number of atoms may even take several days due to calculation capability limits of workstation computers. On the other hand, users need to use more powerful workstations and parallel computer grids which are too expensive to buy easily for reducing the calculation time. In literature, many researchers remark this calculation time problem in their studies. General view of the researchers who studied on geometry optimization using DFT can be summarized as “DFT calculations are time consuming”.

Many researchers study on CNT to obtain perfect CNTs and widen their application areas: Some of the studies are focused on geometry optimizations of the CNTs (Kanamitsu and Saito, 2002; Kürti *et al.*, 2003; Moradian *et al.*, 2008, 2009; Yagi *et al.*, 2004). Also many of the researchers that study on CNT calculations, incorporate artificial intelligence methods into their works (Abo-Elhadeed, 2012; Akbari *et al.*, 2014; Cheng *et al.*, 2015; Ensafi *et al.*, 2010; Hassanzadeh *et al.*, 2015; Hayati *et al.*, 2010; Rahimi-Nasrabadi *et al.*, 2015; Salehi *et al.*, 2016; Shanbedi *et al.*, 2013). Nowadays, this incorporation trend has been increasing (Acı and Avcı, 2016).

The motivation of this research is to reduce the calculation time for atomic coordinates from days to minutes. It is known that the current mathematical methods cannot reduce the calculation time up to this level. In this work, the problem is investigated in another perspective. Instead of calculation; the atomic coordinates are predicted as accurately as possible in a short time. These predicted atomic coordinates can be used as initial coordinates for the simulation software as depicted in Fig. 1. Thus, the exact atomic coordinates can be calculated within minutes or hours instead of days utilizing the proposed approach. In some researches predicted atomic coordinates may be enough in accuracy. In that case, the predicted coordinates may provide the fastest solution.

The main objective aimed in this work is to develop prediction models using regression-based supervised artificial intelligence techniques such as Adaptive-Network Based Fuzzy Inference System (Jang, 1993) (ANFIS), four types of Artificial Neural Network (Gupta, 2013) (ANN) (i.e. Feed Forward Neural Network (FFNN), Function Fitting Neural Network (FITNET), Cascade-Forward Neural Network (CFNN) and Generalized Regression Neural Network (GR

NN)), Classification and Regression Tree (Lawrence and Wright, 2001) (CART) and Support Vector Regression (Smola and Vapnik, 1997) (SVR) to estimate

the atomic coordinates of CNTs. One statistical method (i.e. Multiple Linear Regression (Eberly, 2007) (MLR)) is used to compare results with artificial intelligence based methods.

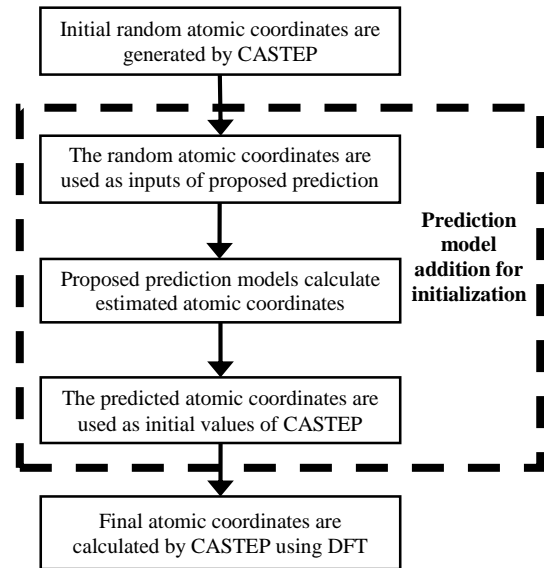


Fig. 1. Steps of the two-staged CASTEP simulation

2. MATERIALS AND METHODS

2.1. Dataset

Two distinct datasets named as input dataset and output dataset are prepared to be used in prediction models. Initial atomic coordinates u, v, w and the pair of integers (n, m) used for specifying the chiral vector are the 5 parameters of input dataset. On the other hand, calculated atomic coordinates u', v', w' are the 3 parameters of output dataset. The dataset consisting of 10,721 data samples firstly is divided randomly into training, validating and testing data randomly, in which there are 70–15–15% training, validating and testing sets respectively. A summary of the descriptive statistics for the dataset is given in Table 1. These statistics include minimum, maximum, mean and standard deviation values of the dataset.

Table 1. Descriptive statistics for the dataset

	Inputs					Outputs		
	u	v	w	m	n	u'	v'	w'
Minimum	0.0451	0.0451	0	2	1	0.0385	0.0389	0
Maximum	0.9548	0.9548	0.9999	12	6	0.9614	0.9610	0.9996
Mean	0.5000	0.5000	0.4994	8.2252	0.3378	0.5000	0.4999	0.4993
Standard Deviation	0.2900	0.2900	0.2900	2.1400	1.6800	0.2909	0.2910	0.2884

The datasets used in this study are generated with CASTEP (2016) using CNT geometry optimization. Different chiral vectors are used for each CNT simulation. The atom type is selected as carbon, bond length is used as 1.42 Å (default value), and then the nanotube is built by CASTEP.

CASTEP uses a parameter named as elec_energy_tol (electrical energy tolerance) which represents that the change in the total energy from one iteration to the next

remains below some tolerance value per atom for a few self-consistent field steps to finalize the computation. This parameter also determines the calculation level of inputs and outputs. The default value of the parameter is 1×10^{-5} eV per atom and is usually suitable (CASTEP, 2016).

Initial coordinates of all carbon atoms are generated randomly. The number of simulated atoms ranges from 32 to 588. The calculation time according to these calculations are approximately varies from 10 minutes to 5 days. These calculation times will take weeks and months for higher atom numbers. All calculations are run on a workstation that has a 2.0 Ghz power on 2 Xeon processors with 4 cores and 8 GB of RAM, using all cores under Linux operating system. The calculation time according to these calculations are approximately varies from 10 minutes to 5 days as given in Table 2 in seconds. These calculation times will take weeks and months for higher atom numbers.

Table 2. The calculation time for CNT simulations in seconds

ID of CNT	Number of Atoms	Calculation Time (Seconds)
1	28	1050.14
2	52	1256.40
3	76	2254.18
4	84	2816.61
5	56	834.04
6	148	18496.07
7	124	33280.80
8	156	9604.28
9	196	59998.78
10	244	19389.07
11	172	64102.59
12	104	7207.22
13	84	6842.67
14	152	7715.19
15	364	78421.39
16	228	13513.07
17	268	27799.53
18	316	35982.11
19	372	94767.02
20	436	266027.27
21	508	233190.94
22	292	27792.55
23	168	13292.91
24	388	106542.26
25	112	6838.91
26	516	201214.72
27	296	34136.32
28	364	103759.38
29	412	95275.60
30	156	9558.96
31	532	427956.63
32	228	27392.57
33	444	159893.39
34	248	74997.74
35	312	40999.97
36	140	10014.92
37	392	83173.05
38	588	397369.36
39	344	89653.65
40	252	26127.05
41	208	23123.48
42	168	11826.42

2.2. Prediction Models

ANFIS, FFNN, FITNET, CFNN, GRNN, CART, SVR and MLR models were trained and tested with the dataset of atomic coordinates for CNTs.

A Sugeno-type (Takagi and Sugeno, 1985) Fuzzy Inference System (FIS) is used by MATLAB's implementation of ANFIS. An adaptive neural network technique is used to train the Sugeno-type FIS parameters. Inputs are mapped through input membership functions and associated parameters by ANFIS. Then through output membership functions and associated parameters to outputs, can be used to interpret the input/output map. The parameters associated with the membership functions change through the learning process. A gradient vector facilitates the computation of these parameters. A measure of how well the FIS is modeling the input/output data for a given set of parameters is provided by this gradient vector. When the gradient vector is obtained, any of several optimization routines can be applied in order to adjust the parameters to reduce some error measure. The sum of the squared difference between actual and desired outputs usually defines this error measure. Either back propagation or a combination of least squares estimation and backpropagation for membership function parameter estimation is used by ANFIS (MATLAB, 2016).

A matrix of training data forms the input training data and last column is the target output data. Test input data is used also in the same way. While the fuzzy toolbox provides many membership function types, Generalized Bell-Shaped Membership Function (gbellmf), Gaussian Curve Membership Function (gaussmf) and Pi-Shaped Membership Function (pimf) performed the best for the prediction of atomic coordinates. After the five inputs enter the ANFIS then they processed for the u' coordinate prediction. Similar FIS models are also designed for prediction of v' and w' coordinates.

FFNN, FITNET and CFNN models have 3 layers (input, hidden and output) and the input and output layers have 5 and 3 neurons respectively. The hidden layers of FITNET and CFNN have 10 neurons and that of FFNN has 20 neurons. A log-sigmoid activation function (LOGSIG) is used in FFNN model and the hyperbolic tangent sigmoid activation function (TANSIG) is used in FITNET and CFNN models in the hidden layer. A pure-linear activation function is used in all models in the output layer and Levenberg-Marquardt algorithm (Moré, 1978) is utilized for training the networks. Weights and biases were randomly initialized. The other important parameters of the FFNN and FITNET models are the number of epochs (1000), the learning rate (0.02), and momentum (0.5). The network parameters have been optimized by try-and-error (i.e. after testing the neural network with several different configurations and observing that these numbers yield the lowest error rates for prediction) in order to reach the accurate results. The parameter σ of GRNN model (also called 'spread' in MATLAB) determines the generalization capability of the GRNN. The best spread parameter is adopted as 2 through this work.

CART analysis was performed using "classregtree" function which specifies some optional parameters in MATLAB. The "prune" option computes the full tree and prunes the subtrees. The "minparent" option splits impure nodes which have k or more observations to be split for given number of k. The "qetoler" option defines tolerance on quadratic error per node for CART. Splitting nodes stops when quadratic error per node drops below qetoler*qed, where qed is the quadratic error for the entire data computed before the decision tree is grown. The

“mergeleaves” option merges leaves that originate from the same parent node and give the sum of risk values greater or equal to the risk associated with the parent node. The values of the parameters were chosen as $\text{prune}=\text{on}$, $\text{minparent}=50$ (default is 10), $\text{qetoler}=1\text{E-}7$ (default is $1\text{E-}6$), $\text{mergeleaves}=\text{on}$. All of the parameter values were decided by trial-and-error.

SVR model was designed by running “fitsvm” function in MATLAB. Several combinations have been tried and Radial Basis Function was chosen as the kernel for performance comparison.

MLR prediction model is designed with the purpose of comparing Machine Learning methods with a statistical regression method. The model is coded in Statistics and Machine Learning Toolbox of MATLAB using “fitlm” function. Model specification is specified as “linear” and model specification equations are set for each coordinate for the predictions of coordinates such as ‘u’ $\sim u+v+w+m+n$ is set for u’; ‘v’ $\sim u+v+w+m+n$ is set for v’; and ‘w’ $\sim u+v+w+m+n$ is set for w’.

3. RESULTS AND DISCUSSION

Mean Squared Error (MSE), Mean Absolute Error (MAE), Standard Error of Estimation (SEE) and Multiple Correlation Coefficient (R) are calculated to evaluate the performance of prediction models. Summaries of mathematic equations of these performance measures are given in Eq. (2), Eq. (3), Eq. (4) and Eq. (5) respectively (Witten and Frank, 2005).

$$MSE = \frac{1}{n} [\sum_{i=1}^n (O_i - P_i)^2] \quad (2)$$

$$MAE = \frac{1}{n} \sum_{i=1}^n |O_i - P_i| \quad (3)$$

$$SEE = \sqrt{1 - \frac{\sum_{i=1}^n (O_i - P_i)^2}{n}} \quad (4)$$

$$R = \sqrt{1 - \frac{\sum_{i=1}^n (O_i - P_i)^2}{\sum_{i=1}^n (O_i - O_m)^2}} \quad (5)$$

where n is the number of data points used for testing, P_i is the predicted value, O_i is the observed value and O_m is the average of the observed values. MATLAB (R2015b 64 bit) (MATLAB, 2016) was utilized for designing proposed models and obtaining performance measures.

Table 3, Table 4 and Table 5 summarize the performance results of u’, v’ and w’ coordinates prediction using ANFIS, FFNN, FITNET, CFNN, GRNN, SVR, CART and MLR models respectively.

Table 3. Performance results of u’ coordinate prediction (the best results are outlined in bold).

Models	Performance metrics			
	MSE	MAE	SEE	R
ANFIS	1.077E-05	2.224E-03	3.282E-03	9.999E-01
FFNN	9.879E-06	2.084E-03	1.000E+00	9.999E-01
FITNET	1.130E-05	2.143E-03	1.000E+00	9.999E-01
CFNN	9.403E-06	2.025E-03	1.000E+00	9.999E-01
GRNN	7.911E-03	2.532E-01	1.000E+00	9.371E-01
SVR	5.102E-04	1.957E-02	9.998E-01	9.970E-01
CART	2.471E-05	3.868E-03	1.000E+00	9.999E-01
MLR	1.525E-01	2.482E+00	3.000E+00	5.999E-01

Table 4. Performance results of v’ coordinate prediction (the best results are outlined in bold).

Models	Performance Metrics			
	MSE	MAE	SEE	R
ANFIS	1.101E-05	2.294E-03	3.318E-03	9.999E-01
FFNN	7.307E-06	1.870E-03	1.000E+00	9.999E-01
FITNET	8.708E-06	1.997E-03	1.000E+00	9.999E-01
CFNN	8.537E-06	1.965E-03	1.000E+00	9.999E-01
GRNN	7.995E-03	2.554E-01	1.000E+00	9.298E-01
SVR	4.985E-04	1.940E-02	9.998E-01	9.971E-01
CART	2.484E-05	3.835E-03	1.000E+00	9.998E-01
MLR	1.298E-01	2.300E+00	3.000E+00	6.000E-01

Table 5. Performance results of w’ coordinate prediction (the best results are outlined in bold).

Models	Performance Metrics			
	MSE	MAE	SEE	R
ANFIS	4.962E-08	1.534E-04	2.228E-04	1.000E+00
FFNN	5.501E-08	1.531E-04	1.000E+00	1.000E+00
FITNET	5.554E-08	1.523E-04	1.000E+00	1.000E+00
CFNN	5.418E-08	1.498E-04	1.000E+00	1.000E+00
GRNN	8.088E-03	2.466E-01	9.587E-01	9.313E-01
SVR	4.321E-04	1.832E-02	9.997E-01	9.983E-01
CART	2.140E-05	3.021E-03	1.000E+00	9.999E-01
MLR	4.865E-02	1.476E-01	3.000E+00	6.000E-01

All models performed good levels of successes when we look at all results with a general view. However, the results of ANFIS, FFNN, FITNET and CFNN models have a superiority over other models. This implies that ANN based models can closely estimate atomic coordinates of CNTs. CART and SVR models produced average performance results comparing to other models. The results can be analyzed in detail as follows:

- CFNN model has the best performance values for u’ and w’ coordinates prediction by means of MSE and MAE. However, MSE and R results of ANFIS, FFNN and FITNET models are very close to CFNN model.
- The best SEE results are achieved by ANFIS model for all coordinates.
- R value prediction results varies in a very small range (from 9.298E-01 to 1.000E+00) for all models except MLR based model.
- MLR based model yielded the worst performance results for all coordinates.
- The estimation results with the highest accuracy are yielded for w’ coordinate (MSE results of the first four models are almost zero).

The results obtained from this study can be used in two ways: i) The predicted atomic coordinates can be used in physical calculations without using a simulation software, ii) The estimated results can be used as an initial value of simulation software for reducing duration of the atomic coordinate calculation seriously.

4. CONCLUSION

As a result of this work, the effectiveness of artificial intelligence based solutions, which estimate atomic coordinates that can be integrated into software, has been observed and the results that have significantly shortened the simulation processes in the field of nanotechnology have been presented to be integrated into scientific or commercial software.

ACKNOWLEDGMENTS

We would like to thank Çukurova University Scientific Research Projects Center for supporting this work (Project code: FDK-2015-3170).

REFERENCES

Abo-Elhadeed, A. F. (2012). "Modeling carbon nanotube transistors using neural networks approach." *Proc., International Conference on Synthesis, Modeling, Analysis and Simulation Methods and Applications to Circuit Design (SMACD)*, pp. 125-128.

Acı, M. and Avcı, M. (2016). "Artificial neural network approach for atomic coordinate prediction of carbon nanotubes." *Applied Physics A*, vol. 7 No. 122, pp. 1-14.

Akbari, E., Buntat, Z., Enzevae, A., Ebrahimi, M., Yazdavar, A. H. and Yusof, R. (2014). "Analytical modeling and simulation of I-V characteristics in carbon nanotube based gas sensors using ANN and SVR methods." *Chemometrics and Intelligent Laboratory Systems*, Vol. 137, No. 1, pp. 173-180.

CASTEP Biovia Materials. <http://accelrys.com/products/collaborative-science/biovia-materials-studio/quantum-catalysis-software.html> [Accessed 10 May 2017].

Cheng, W., Cai, C., Luo, Y., Li, Y. and Zhao, C. (2015). "Mechanical properties prediction for carbon nanotubes/epoxy composites by using support vector regression." *Modern Physics Letters B*, Vol. 29, No. 05, pp. 1550016.

Eberly, L. E. (2007). *Multiple linear regression. In: Topics in biostatistics*, Humana Press, Totowa, NJ, USA.

Ensafi, A. A., Taei, M., Khayamian, T. and Hasanpour, F. (2010). "Simultaneous voltammetric determination of enrofloxacin and ciprofloxacin in urine and plasma using multiwall carbon nanotubes modified glassy carbon electrode by least-squares support vector machines." *Analytical Sciences*, Vol. 26, No. 7, pp. 803-808.

Gupta, N. (2013). "Artificial neural network." *Network and Complex Systems*, Vol. 3, No. 1, pp. 24-28.

Hassanzadeh, Z., Kompany-Zareh, M., Ghavami, R., Gholami, S. and Malek-Khatibi, A. (2015). "Combining radial basis function neural network with genetic algorithm to QSPR modeling of adsorption on multi-walled carbon nanotubes surface." *Journal of Molecular Structure*, Vol. 1098, No. 1, pp. 191-198.

Hayati, M., Rezaei, A. and Seifi, M. (2010). "CNT-MOSFET modeling based on artificial neural network: Application to simulation of nanoscale circuits." *Solid-State Electronics*, Vol. 54, No. 1, pp. 52-57.

Jang, J.-S. (1993). "ANFIS: adaptive-network-based fuzzy inference system." *IEEE Transactions on Systems, Man, and Cybernetics*, Vol. 23, No. 3, pp. 665-685.

Kanamitsu, K. and Saito, S. (2002). "Geometries, electronic properties, and energetics of isolated single walled carbon nanotubes." *Journal of the Physical Society of Japan*, Vol. 71, No. 2, pp. 483-486.

Kohn, W. and Sham, L. J. (1965). "Self-consistent equations including exchange and correlation effects." *Physical review*, Vol. 140, No. 4A, pp. A1133-A1138.

Kürti, J., Zólyomi, V., Kertesz, M. and Sun, G. (2003). "The geometry and the radial breathing mode of carbon nanotubes: beyond the ideal behaviour." *New Journal of Physics*, Vol. 5, No. 1, pp. 125.

Lawrence, R. L. and Wright, A. (2001). "Rule-based classification systems using classification and regression tree (CART) analysis." *Photogrammetric Engineering and Remote sensing*, Vol. 67, No. 10, pp. 1137-1142.

MATLAB. <https://www.mathworks.com/> [Accessed 12 May 2017].

Moradian, R., Behzad, S. and Chegel, R. (2008). "Ab initio density functional theory investigation of structural and electronic properties of silicon carbide nanotube bundles." *Physica B: Condensed Matter*, Vol. 403, No. 19, pp. 3623-3626.

Moradian, R., Behzad, S. and Chegel, R. (2009). "Ab initio density functional theory investigation of Li-intercalated silicon carbide nanotube bundles." *Physics Letters A*, Vol. 373, No. 26, pp. 2260-2266.

Moré J.J. (1978). *The levenberg-marquardt algorithm: implementation and theory. In: Numerical analysis*, Springer, Berlin, Germany.

Rahimi-Nasrabadi, M., Akhoondi, R., Pourmortazavi, S. M. and Ahmadi, F. (2015). "Predicting adsorption of aromatic compounds by carbon nanotubes based on quantitative structure property relationship principles." *Journal of Molecular Structure*, Vol. 1099, No. 1, pp. 510-515.

Salehi, E., Abdi, J. and Aliei, M. H. (2016). "Assessment of Cu (II) adsorption from water on modified membrane adsorbents using LS-SVM intelligent approach." *Journal of Saudi Chemical Society*, Vol. 20, No. 2, pp. 213-219.

Shanbedi, M., Jafari, D., Amiri, A., Heris, S. Z. and Baniadam, M. (2013). "Prediction of temperature performance of a two-phase closed thermosyphon using artificial neural network." *Heat and Mass Transfer*, Vol. 49, No. 1, pp. 65-73.

Smola, A. and Vapnik, V. (1997). "Support vector regression machines." *Advances in Neural Information Processing Systems*, Vol. 9, No. 1, pp. 155-161.

Takagi, T. and Sugeno, M. (1985). "Fuzzy identification of systems and its applications to modeling and control." *IEEE Transactions on Systems, Man, and Cybernetics*, Vol. SMC-15, No. 1, pp. 116-132.

Witten, I. H. and Frank, E. (2005). *Data mining: practical machine learning tools and techniques*, Morgan Kaufmann, San Francisco, USA.

Yagi, Y., Briere, T. M., Sluiter, M. H., Kumar, V., Farajian, A. A. and Kawazoe, Y. (2004). "Stable geometries and magnetic properties of single-walled carbon nanotubes doped with 3 d transition metals: A first-principles study." *Physical Review B*, Vol. 69, No. 7, pp. 075414.

Copyright © Turkish Journal of Engineering (TUJE).
All rights reserved, including the making of copies
unless permission is obtained from the copyright
proprietors.

Turkish Journal of Engineering



Turkish Journal of Engineering (TUJE)
Vol. 2, Issue 3, pp. 125-129, September 2018
ISSN 2587-1366, Turkey
DOI: 10.31127/tuje.403215
Research Article

INVESTIGATION OF ULEXITE USAGE IN AUTOMOTIVE BRAKE FRICTION MATERIALS

Banu Sugözü *¹

Mersin University, Faculty of Engineering, Department of Mechanical Engineering, Mersin, Turkey
ORCID ID 0000-0002-7798-2677
banusugozu@mersin.edu.tr

* Corresponding Author

Received: 08/03/2018

Accepted: 04/05/2018

ABSTRACT

The automotive brake pads are multi-component composites made up of many materials. There are many studies in the literature exploring the use of many different materials in brake pads. In this study, the use of ulexite which is a commercially valuable derivatives of boron that 65% of the total world reservations exists in Turkey were researched for brake pad material. For this purpose, three brake pad specimens containing ulexite differing in amount (3, 6 and 9 wt.%) were produced by a conventional procedure for a dry formulation following dry-mixing, pre-forming and hot pressing. The density of the specimens was determined based on Archimedes principle in water. The surface hardness of all brake pad specimens was measured using Rockwell hardness tester. The friction performance of the brake pad specimens was determined using a real brake disc-type tester with grey cast iron. The weights of each specimen were taken before and after the friction test, and the specific wear rate was determined in accordance to the TSE 555 (1992) standard. The results showed that all specimens are applicable to the industry, consistent with the literature and suitable to the TS 555 standard. Also, the results indicated that ulexite is an ideal material for brake pads.

Keywords: *Ulexite, Brake Lining, Wear, Friction*

1. INTRODUCTION

Boron is an important mineral used in many fields, including nuclear industry, fertilizer industry, the pharmaceutical industry, chemical industry, and automobile industry. Turkey has 65% of the boron reserves in all over the world and manages 32% of the total production (Çalık, 2002). Although boron minerals are used directly in some structures, most of which is processed in factories and converted into the high value-added refined boron derivatives. Some of the commonly used commercial boron derivatives are borax, colemanite, ulexite, kernite, probertite and szaibelyite (Özkan *et al.*, 1997).

With the development of automotive technology, the motor forces, speed of movement and the acceleration capabilities of vehicles have increased compared to the past. This has increased the importance of reliably controlling the movements of the vehicles. The most important safety feature of a car is the brake system. Brake pads are the indispensable parts of the brake systems, being the composite materials that are made up of a combination of many materials with different functions. Although many studies on brake friction materials are presented in the literature, studies investigating the use of boron products in brake pads are relatively few. Sugözü (2009) produced the brake pad specimens using ulexite, colemanite, boric acid and borax pentahydrate which are boron derivatives, and then examined the properties of the produced brake pads including the friction, wear, and resistance. Wannik *et al.* (2012), investigated the effects of boron additives on brake pads and found that boron additives have higher friction performance. Kuş *et al.* (2016), investigated the effect of the amount of colemanite on friction-wear properties of 'the volatile ash reinforced bronze matrix brake pad materials' produced by the hot pressing method, and stated that the friction coefficient of the materials with 0.5% colemanite supplement was higher.

In the present study, the usability of ulexite in brake pad materials was investigated experimentally. For this purpose, the brake pad specimens containing 3%, 6% and 9% ulexite were produced by the powder metallurgy method. The density of specimens was determined according to the Archimedes principle and the hardness was determined using the Rockwell hardness tester device (HRL). For friction performance tests, a full-scale brake pad device with grey cast iron disk was used. The specific wear rate was calculated according to the TSE 555 standard by determining the weights of each specimen before and after testing.

2. MATERIALS AND METHODS

The production parameters of the materials and specimens used in brake pads have a significant impact on the brake performance. We determined the materials and production conditions according to the previous studies in the literature. The materials used in the specimens are given in Table 1 in mass percentages. U3, U6, and U9 are specimen codes; U refers ulexite, and its number also refers to the percentage in the composition.

Table 1. Contents of specimens (mass %)

The task of the material	Type of material	U3	U6	U9
Binding material	Phenolic resin	20	20	20
Reinforcing material	Steel wool	5	5	5
Friction modifiers	Cashew powder	10	10	10
	Brass shavings	5	5	5
Metallic shavings	Copper shavings	6	6	6
	Graphite	3	3	3
Solid lubricant	Graphite	3	3	3
Abrasive	Alumina	8	8	8
Friction modifiers	Ulexite	3	6	9
Filling material	Barite	40	37	34

Prior to the production process, the particle size of each material forming the contents of brake pad was primarily determined with the help of sieves shown in Fig. 1 (a). Then, the amount of each material forming the brake pad content was determined by 0.001 g precision scale shown in Fig. 1 (b) and transferred to the powder chamber shown in Fig. 1 (c) for mixing. In order to ensure homogeneity of the mixture, the specimen content was mixed at 150 rpm for 10 minutes on the specially produced powder mixing device shown in Fig. 1 (d). The resulting mixture was carefully placed in the 25.4 mm diameter cold press mold shown in Fig. 1 (e). While doing this, care has been taken not to spread the dust around due to sudden movements. The dust was pressed under 8000 kPa pressure for 2 minutes. The final product was obtained by removing the cold pressed specimens from the mold and placing them in the hot press mold shown in Fig. 1 (f) and pressing them for 12 minutes under 10000 kPa pressure at 150 °C.

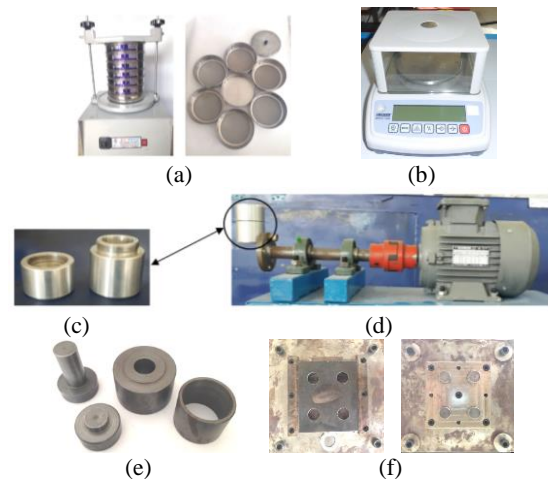


Fig. 1. The materials used in the production of specimens (a) the sieve-shaker and sieves (b) the precision scales (c) the powder chamber (d) the powder mixing device (e) the cold press mold (f) the hot press mold

The density of the specimens was determined according to the Archimedes principle and the hardness was determined using the Rockwell hardness tester

device (HRL). During the hardness measurement process, a preload of 10 kgf and a full load of 60 kgf was applied with a steel ball in diameter 6.35 mm at the submersible end (Başar *et al.*, 2017). Hardness measurements were taken from the frictional surface of the specimens. A full-scale brake pad test device with grey cast iron disc having a diameter of 280 mm and hardness of 116 HB, whose schematic drawing is shown in Fig. 2, was used to determine the abrasion and friction properties of the specimens. The device can be fully controlled by a computer and includes data collection software. The specific wear rate was calculated according to the TSE 555 standard by determining the weights of each specimen before and after testing.

During the experiments, the temperature increases due to friction between the disk and the brake pad. In order to investigate the effect of temperature increase on the performance of the brake pad, the non-contact thermometer measured the surface temperature of the brake pad at a distance of about 2 cm from the friction surface to the disc. A digital thermometer was used to measure temperature. The surface temperature of the disc is automatically transferred to the computer environment in seconds during the experiment (Sugözü, 2016).

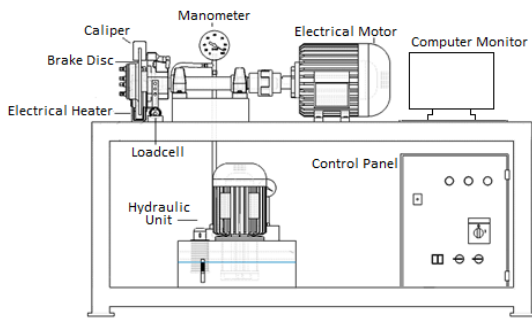


Fig. 2. Brake pad test device (Sugözü, 2015)

The coefficient of friction and wear of specimens was obtained by conducting experiments as specified in the TS 555 (1992) and TS 9076 standard (1991). In experimental conditions, first of all, 310 rpm, 700 kPa pressure, and a temperature not exceeding 100 °C were provided; and then the grinding process was applied, until the surface contact of the specimen to the disc is at least 95%. Thus, the surface got ready for the experiment. Then the tests were completed with the pressure of 1050 kPa and speed of 6 m/s for 30 minutes.

3. RESULTS

The coefficient of friction for automotive brake pads is the most important parameter affecting the brake performance. The coefficient of friction-temperature-time graphs of specimens are given in Fig. 3 for U3 coded specimens, and in Fig. 4 for U6 coded specimens, and also in Fig. 5 for U9 coded specimens. In figures, the coefficient of friction was low at the initial of the test because the applied pressure does not influence suddenly but gradually. Sudden pressure application will cause damage to the brake pads, so the pressure was gradually increased. In addition, at the initial of the test, the disc and the brake pad are in the running-in period (grinding) and the friction layers in which the friction force is effective

are not yet formed (Sugözü, 2016). Therefore, there is a continuous change in the coefficient of friction. In the literature, this situation has been reported to occur with the transition of heat to the inner part of the contact areas on the surface of the disc during friction (Anderson, 1992). Another explanation is that the adhesion on the surface roughness of the friction couples results in the repetition of the adhesion-release, causing fluctuations in the coefficient of friction (Stachowiak and Batchelor, 2001).

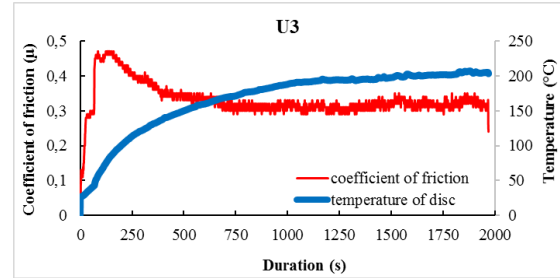


Fig. 3. The coefficient of friction and temperature graph of the specimen containing 3% ulexite, according to the friction time

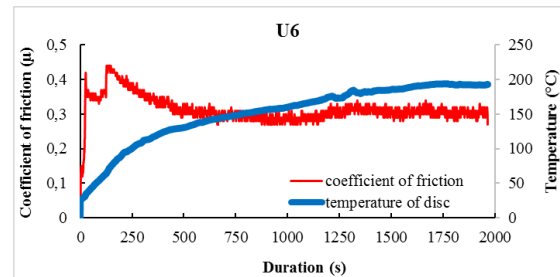


Fig. 4. The coefficient of friction and temperature graph of the specimen containing 6% ulexite, according to the friction time

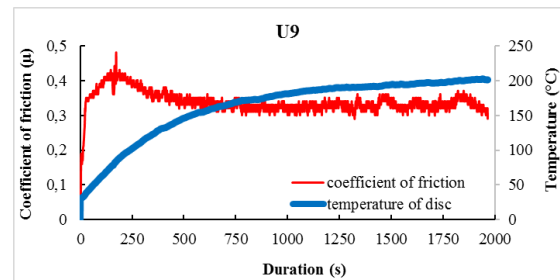


Fig. 5. The coefficient of friction and temperature graph of the specimen containing 9% ulexite, according to the friction time

Fig. 3 shows the coefficient of friction and temperature graph of the specimen containing 3% ulexite, according to the friction time. The highest coefficient of friction obtained during the tests was 0.47, and the highest temperature was 206.8 °C. Fig. 4 shows the coefficient of friction and temperature graph of the specimens containing 6% ulexite, according to the friction time. During the tests, the highest temperature occurred between the disk and brake pad is 193.3 °C. The highest coefficient of friction of the brake pad specimen is 0.44. However, the friction stability was found to be 71%. Fig.

5 represents the coefficient of friction and temperature graph of the specimen containing 9% ulexite. The highest coefficient of friction obtained in the tests is 0.48 °C, and the highest temperature between the disc and brake pad is 202 °C. The friction stability was calculated as 70%. According to the literature, the friction stability (%) should be as high as possible and close to 100, the slope and fluctuations of the obtained curve should be low level (Bijwe *et al.*, 2012). It is desirable that the coefficient of friction of the automotive brake pads is high, the wear is low and the friction stability is stable. Physical and tribological properties of specimens are shown in Table 2 and Table 3.

Table 2. Tribological properties of specimens

Specimen Code	Specific wear rate (cm ³ /Nm)	The average coefficient of friction
U3	2.054×10^{-6}	0.331
U6	2.109×10^{-6}	0.313
U9	1.893×10^{-6}	0.337

Table 3. Physical properties of specimens

Specimen Code	Rockwell hardness (HRL)	Density (g/cm ³)
U3	81	1.9
U6	88	2.16
U9	90	2.22

Table 3 shows that the hardness and density of the specimens are increased by increasing the amount of ulexite in the composite. Considering the average coefficient of friction and the specific wear rate, it was found that the specimen containing 9% ulexite was better. The coefficient of friction of the specimens is obtained by dividing the coefficient of friction by the highest coefficient of friction obtained during the test and expressed as a percentage.

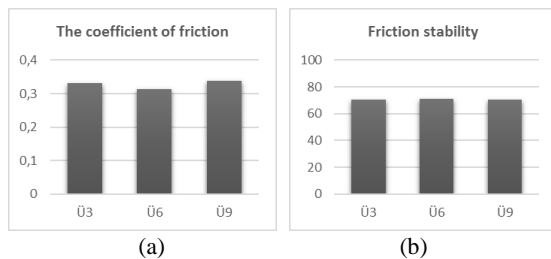


Fig. 6. (a) The coefficient of friction (b) friction stability graphs of specimens

4. CONCLUSION

In this study, the usability of ulexite, which is a boron mineral, in automotive brake pads was investigated by experimental studies. Three different specimens containing 3%, 6% and 9% ulexite were prepared for this purpose. A full-scale brake pad device was used for the wear and friction tests of the specimens. The results obtained from the tests are summarized below;

- The highest average coefficient of friction value for all specimens undergo friction test is 0.337, belonging to the U9-coded specimen containing 9% ulexite, the lowest

average friction coefficient is 0.313, belonging to the U6-coded specimen containing 6% ulexite.

- It was reported that as the amount of ulexite increased, the hardness and density increased. The direct proportion between the hardness and density was determined to be consistent with the literature.

- The friction stability of specimens was observed to be almost the same for each specimen, and it was concluded that the friction stability does not depend on the amount of ulexite content.

- According to the results obtained from the friction and abrasion tests, all specimens can be utilized in the industry in accordance with the literature and conform to the TS 555 standard. Accordingly, ulexite which is a boron derivative could be used as an alternative material in automotive brake pads.

REFERENCES

Anderson, A. E. (1992). ASM handbook, Friction, lubrication, and wear technology 18, pp. 569-577.

Başar, G., Buldum, B.B., Sugözü, İ. (2017). "Effects of Colemanite and Ulexite on the Tribological Characteristics of Brake Friction Materials." *Proc., International Advanced Researches & Engineering Congress*, Osmaniye, Turkey, pp. 87-94.

Bijwe, J., Aranganathan, N., Sharma, S., Dureja, N. and Kumar, R. (2012). "Nano-abrasives in friction materials-influence on tribological properties." *Wear*, Vol. 296, No. 1, pp. 693-701.

Çalık, A. (2002). "Turkey boron minerals and features." *Engineer and Machinery*, Vol. 508, pp. 1-9.

Kuş, H., Altıparmak, D. and Başar G. (2016). "The Effect of Colemanite Content on Friction-Wear Properties of the Bronze Based Brake Lining Material Reinforced with Fly Ash Fabricated by the Hot Pressing Method." *Journal of Polytechnic*, Vol. 19, No. 4, pp. 537-546.

Özkan, Ş. G., Çebi, H., Delice, S., and Doğan, M. (1997). "Boron minerals properties and mining." *Proc., 2nd Industrial Minerals Symposium*, İzmir, Turkey, pp. 224-228.

Stachowiak, G.W. and Batchelor, A.W. (2001). *Engineering Tribology*, Heineman, Boston, MA, pp. 36-44.

Sugözü, İ. (2009). Production of non-asbestos automotive brake lining additional boron and investigation of its braking characteristic, PhD Thesis, Fırat University, Elazığ, Turkey.

Sugözü, I. (2015). "Investigation of using rice husk dust and ulexite in automotive brake pads." *Materials Testing*, Vol. 57, No. 10, pp. 877-882.

Sugözü, B. (2016). The effect of additive of nano silica, nano alumina and nano zircon abrasive particles on brake lining properties, PhD Thesis, Selçuk University, Konya, Turkey.

TS 555 (1992). *Highway Vehicles-Brake System-Brake Pads for Friction Brake*, Turkish Standard Institute, Ankara, Turkey.

TS 9076 (1991). *Road Vehicles-Brake Linings-Evaluation of Friction Material Characteristics- Small Sample Bench Test Procedure*, Turkish Standard Institute, Ankara, Turkey.

Wannik, W. B., Ayob, A. F., Syahrullail, S., Masjuki, H. H. and Ahmad M. F. (2012). "The effect of boron friction modifier on the performance of brake pads." *International Journal of Mechanical and Materials Engineering*, Vol. 7, No. 1, pp. 31-35.

Copyright © Turkish Journal of Engineering (TUJE).
All rights reserved, including the making of copies
unless permission is obtained from the copyright
proprietors.

Turkish Journal of Engineering



Turkish Journal of Engineering (TUJE)
Vol. 2, Issue 3, pp. 130-138, September 2018
ISSN 2587-1366, Turkey
DOI: 10.31127/tuje.411549
Research Article

CRITICALITY CALCULATION OF A HOMOGENOUS CYLINDRICAL NUCLEAR REACTOR CORE USING FOUR-GROUP DIFFUSION EQUATIONS

Babatunde Michael Ojo ^{*1}, Musibau Keulere Fasasi ², Ayodeji Olalekan Salau ³, Stephen Friday Olukotun ⁴ and Mathew Ademola Jayeola ⁵

¹ Obafemi Awolowo University, Science Faculty, Physics and Engineering Physics Department, Ile-Ife, Nigeria
ORCID ID 0000-0002-2217-7654
Ojobabatundemichael@gmail.com

² Obafemi Awolowo University, Science Faculty, Center for Energy and Research Development, Ile-Ife, Nigeria
ORCID ID 0000-0002-4056-173X
mfasasi2001@yahoo.com

³ Obafemi Awolowo University, Technology Faculty, Electronic and Electrical Engineering Department, Ile-Ife, Nigeria
ORCID ID 0000-0002-6264-9783
ayodejisalau98@gmail.com

⁴ Obafemi Awolowo University, Science Faculty, Physics and Engineering Physics Department, Ile-Ife, Nigeria
ORCID ID 0000-0002-7409-5466
olukotunsf@gmail.com

⁵ Obafemi Awolowo University, Science Faculty, Physics and Engineering Physics Department, Ile-Ife, Nigeria
ORCID ID 0000-0002-3131-3187
senatormao6@gmail.com

* Corresponding Author

Received: 01/04/2018 Accepted: 04/05/2018

ABSTRACT

In this study, we present a general equation for Finite Difference Method Multi-group Diffusion (FDMMD) equations of a cylindrical nuclear reactor core. In addition, we developed an algorithm which we called TUNTOB for solving the FDMMD equations, determined the fluxes at each of the mesh points and calculated the criticality of the four energy group. This was with a view to using the four-group diffusion equations to estimate the criticality of a cylindrical reactor core that will be accurate and locally accessible for nuclear reactor design in developing countries. The multi-group diffusion equations were solved numerically by discretization using the Finite Difference Method (FDM) to obtain a general equation for a cylindrical reactor core. The fluxes at each mesh point and the criticality of the four energy group were then determined. From the results obtained, we observed that an increment in iteration led to an increase in the effective multiplication factor (k_{eff}) with a corresponding increase in the computation time. A maximum effective multiplication factor was reached when the number of iteration was 1000 and above. Having established the optimal number of iterations, the effects of the mesh sizes on the computation examined revealed that the values of k_{eff} increases as the mesh sizes becomes smaller until an optimal mesh size of 1 x 1 cm² was reached and further decrease in mesh sizes gave no further improvement in the value of k_{eff} . The Study concluded that the accuracy in the values of k_{eff} and the smoothness of the neutron distribution curves in 3-D representations depend on the number of mesh points.

Keywords: Four-group diffusion equation, Effective multiplication factor, Mesh size, Reactor, Criticality calculation

1. INTRODUCTION

The criticality of a system containing fissionable materials is described by its effective multiplication factor (k_{eff}). The effective multiplication factor is the ratio of the number of neutrons in one generation to the number of neutrons in the previous generation as shown in Eq. (1). A generation is essentially the lifetime of a neutron, in a finite system, the effective multiplication factor is denoted as $k_{effective}$ or k_{eff} , which is used to determine the stability of a nuclear reactor core. When a system is critical, it maintains a steady-state chain reaction of nuclear fissioning, and $k_{eff} = 1$. The average neutron population in a critical system stays constant in time. A sub-critical system has $k_{eff} < 1$ and the neutron population dies off in time. The neutron population in a super-critical system, where $k_{eff} > 1$, grows without bound in time (Urbatsch, 1995).

$$k_{eff} = \frac{\text{Number of neutrons in one generation}}{\text{Number of neutrons in the preceding generation}} \quad (1)$$

The knowledge of k_{eff} is necessary when designing nuclear reactors. However, numerical methods are used almost exclusively for criticality calculations (Urbatsch, 1995). Different numerical methods have been proposed to solve the two group neutron diffusion equations with little attention to the other groups. Although, the two group neutron diffusion equations do not give a detailed explanation of neutron flux distribution in a practical nuclear reactor core, the four-group neutron diffusion equations are known to give a far better description of neutron distribution in a practical nuclear reactor core. Hence the study of the criticality of the cylindrical reactor core and its calculation using four-group diffusion equations by applying the finite difference method (FDM).

The remainder of this paper is organized as follows. In Section 2, a review of related works is provided, while a detailed explanation of the discretization of the four group diffusion equations using finite difference method is given in Section 3. In Section 4, the results are presented and discussed and Section 5 concludes this paper.

2. NUCLEAR REACTOR CORE

A nuclear reactor core is a part of a nuclear reactor which contains the nuclear fuel components where all the nuclear reactions takes place and consequently heat is generated from the reaction. In addition, a nuclear reactor produces and controls the release of energy in form of heat from the splitting of the atoms of uranium.

2.1. Neutron-Nucleus Reactions

It is important to recognize that since neutrons are electrically neutral, they are unaffected by the electrons in the atom or by the positive charge of the nucleus. As a consequence, neutrons pass through the atomic electron cloud and interact directly with the nucleus. Neutrons

collide with nuclei, not with atoms (Larmash and Baratta, 2001).

The operation of a reactor basically depends on how neutrons interact with nuclei in the reactor. There are various types of known neutron interactions which could be considered as shown in Fig. 1 (Arzhanov, 2010). All neutron reactions can be categorized as either elastic or inelastic collisions, on the condition that either the kinetic energy is conserved in the collision or not. (Burnham, 1967).

2.1.1. Neutron Flux

Neutron flux is defined as the product of the neutron density and the velocity,

$$\phi = nv \quad (2)$$

so that it is expressed in units of neutrons per cm^2 per second. It is equal to the total distance (sum of all the path lengths) travelled in one second by all the neutrons present in one cm^3 .

In a reactor, the values of neutron density and neutron flux are a function of location in the core. Because the neutron flux is an essential ingredient in the computation of reactor rates, the determination of the spatial distribution of the neutron flux in the core is an important part of reactor physics. The value of the neutron flux at a given point in the core will depend on the distribution of nuclear properties like the cross sections throughout the core, and on the position in relation to the central part of the core and to the external surface of the reactor. The neutron flux continually drops to zero at, or just beyond, the radial and axial boundaries of the core. The behavior of the flux in the core and its rate of decline towards the boundaries must be calculated by means of computer codes (AECBC, 1993; Jayeola *et al.*, 2018).

2.1.2. The Neutron Diffusion Equation

The neutron diffusion equations provide an essential exact description of the neutron distribution within a reactor. Its solution would contain essentially all the information we require concerning the nuclear behavior of the reactor (Duderstadt and Hamilton, 1976).

The multi-group diffusion equation comprises of the groups of neutrons of different energies diffusing within a nuclear reactor. The basic diffusion equation for each group of neutrons is the same, but with absorption generalized to all processes that remove the neutron from the group that is absorption plus scattering to another group and with the source of neutrons for each group specialized to include the in-scattering of neutrons from the other groups, which is also diffusing within the reactor (Stacey, 2007).

2.1.3. Numerical Methods used in neutron diffusion equation

It is assumed that a uniform reactor has the shape of a cylinder of physical radius (R) and height (H). This finite cylindrical reactor has cylindrical geometry which have coordinates at its origin. In order to solve the diffusion equations, the Laplacian is replaced by its

cylindrical form: cylindrical coordinates - 3D, 2D. This is not dependent on angle Θ , therefore, the 3D Laplacian is replaced by its two-dimensional form (2D). This makes it practicable to solve the problem using radial and axial directions. This is because the flux is a function of radius - r and height - z only ($\Phi(r, z)$).

Furthermore, numerical solutions of neutron diffusion equations have been solved using a number of numerical methods such as the finite difference, finite element, nodal and boundary element methods. These methods are all mesh-based in which the nodes that discretize the problem domain are related in a predefined manner (Tanbay and Bilge, 2013). However, numerical methods are used most exclusively for criticality calculations. Criticality calculations k_{eff} are based on power iteration procedures, where different multi-group diffusion equations with a number of iterations are used to estimate the effective multiplication factor (k_{eff}). This iteration process is repeated until the fission distribution has converged.

3. METHODOLOY

3.1. Calculation of the Four-Group Diffusion Equations

To calculate the four-group diffusion equation, we use the finite difference discretization of steady state four-group neutron diffusion equation in a cylindrical coordinate. First, the finite difference discretization of one group differential equation was established and later extended to four-group differential equation. The boundary conditions introduced in this research are: the neutron flux vanishes at the extrapolated boundary of the core ($r = R$ and $z = 0, H$). Where $R =$ Extrapolated Radius and $H =$ Extrapolated Height. The multi-group diffusion system in a cylindrical coordinate can be written as:

$$\begin{aligned} \frac{1}{r} \frac{\partial}{\partial r} \left[D(r, z) r \frac{\partial \varphi(r, z)}{\partial r} \right] + \frac{\partial}{\partial z} \left[D(r, z) \frac{\partial \varphi(r, z)}{\partial z} \right] \\ - \sum_t (r, z) \varphi(r, z) \\ = -S(r, z) \end{aligned} \quad (3)$$

The dependent variable in Eq. (3) is the neutron flux, D is the diffusion coefficient and S is the neutron fission source used to initiate the fission reaction. The third term in Eq. (3), (σ_t subscript 't') is the total macroscopic cross section of the reactor core.

Multiplying Eq. (3) through by r, we obtain:

$$\frac{\partial}{\partial r} \left[D(r, z) r \frac{\partial \varphi(r, z)}{\partial r} \right] + \frac{\partial}{\partial z} \left[r D(r, z) \frac{\partial \varphi(r, z)}{\partial z} \right] - r \sum_t (r, z) \varphi(r, z) = -rS(r, z) \quad (4)$$

The Eq. (4) was discretized using a finite difference method to obtain the four-group diffusion equations by considering the neutron flux varying along the radial and axial coordinate, hence the Fick's law for the radial and axial coordinate can be written as Eqs. (5) and (6) respectively:

$$J = D(r, z) r \frac{\partial \varphi(r, z)}{\partial r} \quad (5)$$

and

$$Y = D(r, z) \frac{\partial \varphi(r, z)}{\partial z} \quad (6)$$

where J and Y are the neutron current density for the radial and axial coordinates respectively. Substituting Eq. (5) and Eq. (6) into Eq. (4), we obtain Eq. (7).

$$\frac{\partial J}{\partial r} + r \frac{\partial Y}{\partial z} - r \sum_t (r, z) \varphi(r, z) = -rS(r, z) \quad (7)$$

The reactor is assumed to cover a special mesh of r and z dimensions as shown in the Fig. 2. Hence Eq. (7) is solved by integrating over the mesh intervals, to obtain:

$$\int_{r_{i-1/2}}^{r_{i+1/2}} \int_{z_{j-1/2}}^{z_{j+1/2}} \frac{\partial J}{\partial r} dr dz + r \int_{r_{i-1/2}}^{r_{i+1/2}} \int_{z_{j-1/2}}^{z_{j+1/2}} \frac{\partial Y}{\partial z} dr dz - r \int_{r_{i-1/2}}^{r_{i+1/2}} \int_{z_{j-1/2}}^{z_{j+1/2}} \sum_t \varphi(r, z) dr dz = \int_{r_{i-1/2}}^{r_{i+1/2}} \int_{z_{j-1/2}}^{z_{j+1/2}} r S g dr dz. \quad (8)$$

Carrying out the integration in Eq. (8), we have:

$$\int_{z_{j-1/2}}^{z_{j+1/2}} (J_{i+1/2} - J_{i-1/2}) dz + \int_{r_{i-1/2}}^{r_{i+1/2}} (Y_{j+1/2} - Y_{j-1/2}) dr = \int_{r_{i-1/2}}^{r_{i+1/2}} \int_{z_{j-1/2}}^{z_{j+1/2}} (\sum_t \varphi - S) dr dz. \quad (9)$$

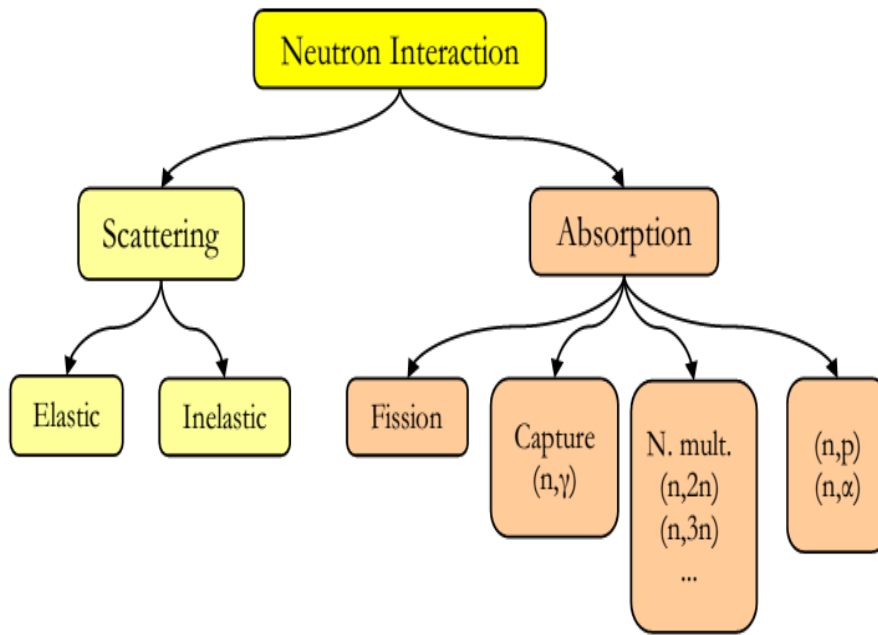


Fig. 1. Types of neutron interaction with matter.

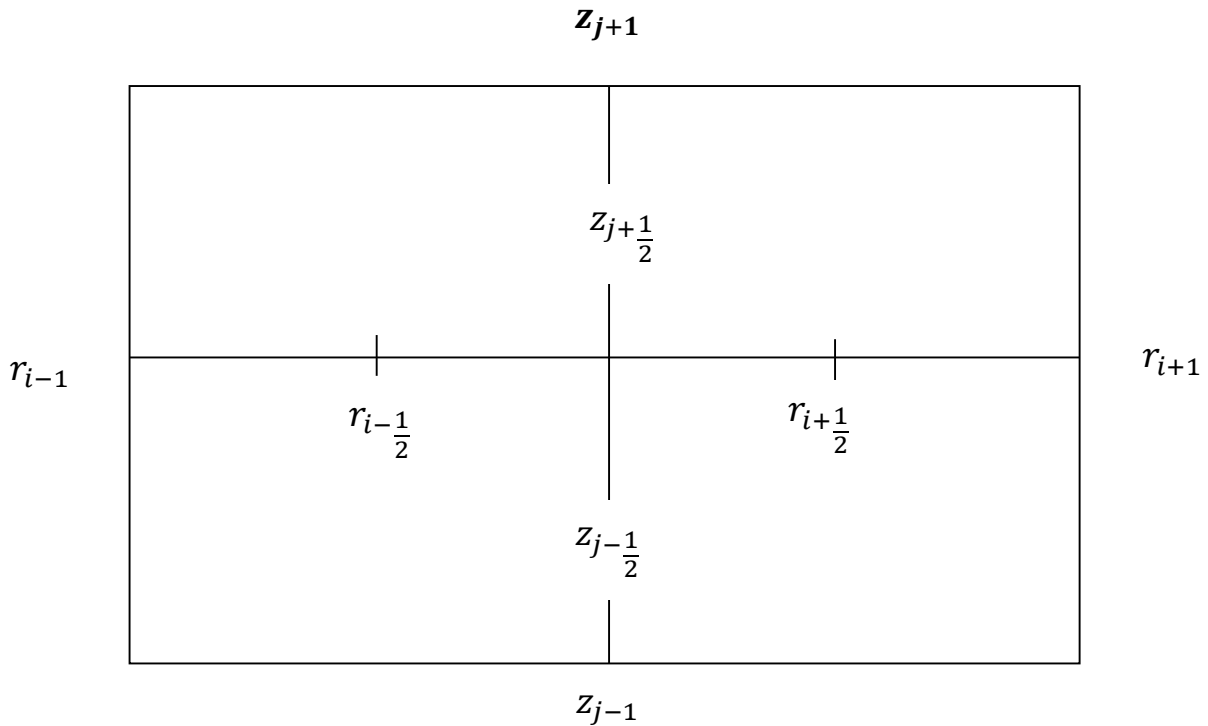


Fig. 2. Spatial mesh used for the finite difference approximation.

Each term in Eq. (9) can be written as Eqs. (10) and (11). Putting Eqs. (10), (11) and (12) into Eq. (9), we obtain Eq. (13). Integrating Eq. (5) over the interval $r_i < r < r_{i+1/2}$; $z_{j-1/2} < z < z_{j+1/2}$ eliminates J whilst an integration of Eq.(6) is performed over the limits $r_{i-1/2} < r < r_{i+1/2}$; $z_j < z < z_{j+1/2}$ eliminates Y. The simplified equation for the parameter J and Y can be written as Eq. (14), (15) and Eq. (16) and (17)

respectively. Putting Eqs. (14), (15), (16) and (17) into Eq. (13), we obtain Eq. (18). On further simplification of Eq. (18) and applying the boundary conditions, we obtain Eq. (19). The finite difference equation for the four-group diffusion equations in a cylindrical geometry can be obtained from Eq. (19). This is written as Group 1 (Eq. 20), Group 2 (Eq. 22), Group 3 (Eq. 23) and Group 4

(Eq. 24) respectively. The obtained four-group diffusion equations is the numerical solution for four-group diffusion equation in a cylindrical reactor core.

Where,

$\Sigma_{s,g \rightarrow g+1}$ (Macroscopic scattering cross section from energy group g to $g + 1$),

D_g (Neutron diffusion coefficient in energy group g),

$\Sigma_{a,g}$ (Macroscopic absorption cross section in energy group g) and

$v\Sigma_{f,g}$ is the source term giving the rate at which source neutrons appear in the group.

$$\int_{z_{j-1/2}}^{z_{j+1/2}} (J_{i+1/2} - J_{i-1/2}) dz = (J_{i+1/2} - J_{i-1/2}) \Delta z_j, \quad (10)$$

$$\int_{r_{i-1/2}}^{r_{i+1/2}} (Y_{j+1/2} - Y_{j-1/2}) dr = (Y_{j+1/2} - Y_{j-1/2}) r_i \Delta r_i, \quad (11)$$

$$\int_{r_{i-1/2}}^{r_{i+1/2}} \int_{z_{j-1/2}}^{z_{j+1/2}} (\Sigma_t \varphi - S) dr dz = (\Sigma_{t,i,j} \Delta r \Delta z)_{i,j} \varphi_{i,j} r_i - (S \Delta r \Delta z)_{i,j} r_i, \quad (12)$$

$$(J_{i+1/2} - J_{i-1/2}) \Delta z_j + (Y_{j+1/2} - Y_{j-1/2}) r_i \Delta r_i - (\Sigma_{t,i,j} \Delta r \Delta z)_{i,j} \varphi_{i,j} r_i = - (S \Delta r \Delta z)_{i,j} r_i. \quad (13)$$

$$J_{i+1/2,j} = \frac{D_{i+1/2,j} r_{i+1/2} \Delta z_j}{\Delta r_{i+1/2} \Delta z_{i+1/2,j}} [\varphi_{i+1,j} - \varphi_{i,j}], \quad (14)$$

$$J_{i-1/2,j} = \frac{D_{i-1/2,j} r_{i-1/2} \Delta z_j}{\Delta r_{i-1/2} \Delta z_{i-1/2,j}} [\varphi_{i,j} - \varphi_{i-1,j}], \quad (15)$$

$$Y_{i,j+1/2} = \frac{D_{i,j+1/2} \Delta r_i}{\Delta r_{i,j+1/2} \Delta z_{j+1/2}} [\varphi_{i,j+1} - \varphi_{i,j}], \quad (16)$$

$$Y_{i,j-1/2} = \frac{D_{i,j-1/2} \Delta r_i}{\Delta r_{i,j-1/2} \Delta z_{j-1/2}} [\varphi_{i,j} - \varphi_{i,j-1}], \quad (17)$$

$$\begin{aligned} & \frac{D_{i+1/2,j} r_{i+1/2} \Delta z_j}{\Delta r_{i+1/2} \Delta z_{i+1/2,j}} (\varphi_{i+1,j} - \varphi_{i,j}) - \frac{D_{i-1/2,j} r_{i-1/2} \Delta z_j}{\Delta r_{i-1/2} \Delta z_{i-1/2,j}} (\varphi_{i,j} - \varphi_{i-1,j}) + \frac{D_{i,j+1/2} r_i \Delta r_i}{\Delta r_{i,j+1/2} \Delta z_{j+1/2}} (\varphi_{i,j+1} - \varphi_{i,j}) \\ & - \frac{D_{i,j-1/2} r_i \Delta r_i}{\Delta r_{i,j-1/2} \Delta z_{j-1/2}} (\varphi_{i,j} - \varphi_{i,j-1}) - r_{i,j} \Sigma_{t,i,j} \varphi_{i,j} \Delta r_i \Delta z_j = -r_{i,j} S_{i,j} \Delta r_i \Delta z_j. \end{aligned} \quad (18)$$

$$\varphi_{i,j} = \frac{2D r_i (\varphi_{i+1,j} + \varphi_{i-1,j} + \varphi_{i,j+1} + \varphi_{i,j-1}) + r_i [S_{i,j}] \Delta r \Delta z}{4D r_i + r_i \Sigma_t}. \quad (19)$$

Group 1:

$$\varphi_{i,j}^1 = \frac{2D^1 r_i (\varphi_{i+1,j}^1 + \varphi_{i-1,j}^1 + \varphi_{i,j+1}^1 + \varphi_{i,j-1}^1) + r_i [S_{i,j}^1]}{4D^1 r_i + r_i \Sigma_{t,i,j}^1}, \quad (20)$$

$$\text{where} \quad \Sigma_{t,i,j}^1 = \Sigma_{a1}, \quad (21)$$

and where the subscript represents the group number,

Group 2:

$$\varphi_{i,j}^2 = \frac{2D^2 r_i (\varphi_{i+1,j}^2 + \varphi_{i-1,j}^2 + \varphi_{i,j+1}^2 + \varphi_{i,j-1}^2) + \Sigma_{1 \rightarrow 2} \varphi_{i,j}^1}{4D^2 r_i + r_i \Sigma_{t,i,j}^2}, \quad (22)$$

$$\text{where} \quad \Sigma_{t,i,j}^2 = \Sigma_{a2} + \Sigma_{1 \rightarrow 2}, \quad (23)$$

Group 3:

$$\varphi_{i,j}^3 = \frac{2D^3 r_i (\varphi_{i+1,j}^3 + \varphi_{i-1,j}^3 + \varphi_{i,j+1}^3 + \varphi_{i,j-1}^3) + \Sigma_{2 \rightarrow 3} \varphi_{i,j}^2}{4D^3 r_i + r_i \Sigma_{ti,j}^3} \quad (24)$$

$$\text{where } \Sigma_{ti,j}^3 = \Sigma_{a3} + \Sigma_{1 \rightarrow 3} + \Sigma_{2 \rightarrow 3}, \quad (25)$$

Group 4:

$$\varphi_{i,j}^4 = \frac{2D^3 r_i (\varphi_{i+1,j}^4 + \varphi_{i-1,j}^4 + \varphi_{i,j+1}^4 + \varphi_{i,j-1}^4) + \Sigma_{3 \rightarrow 4} \varphi_{i,j}^3}{4D^4 r_i + r_i \Sigma_{ti,j}^4}, \quad (26)$$

$$\text{where } \Sigma_{ti,j}^4 = \Sigma_{a4} + \Sigma_{1 \rightarrow 4} + \Sigma_{2 \rightarrow 4} + \Sigma_{3 \rightarrow 4}. \quad (27)$$

Next, TUNTOB proceeds from the first group to the second, third and fourth group, iterating within each group until the criteria convergence is met. It evaluates the tolerance between the old and the new k_{eff} values. To calculate the new k_{eff} , the program integrates the old and new source terms over space and essentially averages them. With the updated source and k_{eff} , the iterations are performed again. The process continues until convergence is met. Next the program checks if the reactor is critical. If k_{eff} is very close to or equal to one (1), the system is critical. If the reactor is not critical, the program will again recommend an adjusted value for the core geometry, guessed multiplication factor (k) and flux.

3.2. Design of the Algorithm (TUNTOB)

The algorithm was designed using Matlab. Matlab was used because its algorithms can be developed in much shorter time than equivalent FORTRAN or C programs (Kiusalaas, 2005). The TUNTOB algorithm was developed for the criticality calculations of a homogenous cylindrical reactor core using four-group diffusion equations. The flow chart of the proposed algorithm is shown in Fig. 3.

4. RESULTS AND DISCUSSION

4.1. Iteration and Mesh Sizes Optimization

4.1.1. Iteration optimization

The calculations of the iteration optimization are shown in Table 1. A maximum of 1000 and a minimum of 600 iterations were performed. The 1000th iteration was performed for a 12 cm x 24 cm mesh size of the reactor core. The Table 1 shows the values of the effective multiplication factor of the same mesh size with the number of iterations (600-1000). It was observed that an increment in iteration leads to an increase in the effective multiplication factor obtained from 0.9983 to 0.9990 with a corresponding increase in the computation time. The maximum effective multiplication factor of ($k_{eff} = 0.9990$) was reached when the number of iterations were 1000 and above. Therefore, it was concluded that the optimal number of iterations required for this calculation is 1000.

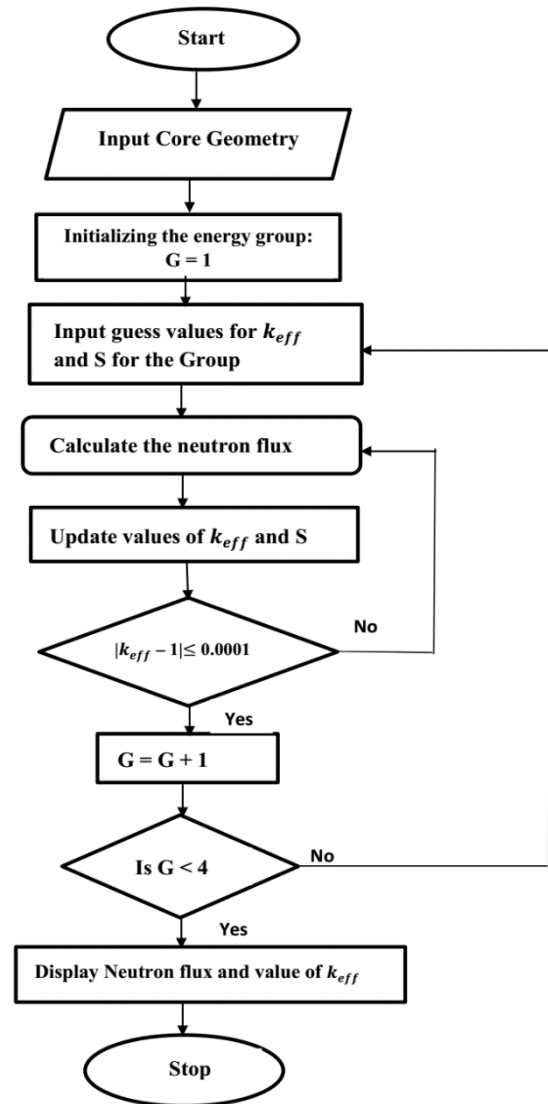


Fig. 3. Flow chart of the proposed algorithm (TUNTOB).

Table 1. Iterations optimization and its corresponding maximum effective multiplication factor (k_{eff}) with constant mesh size (4 cm x 4 cm).

Number of Iteration	Effective Multiplication Factor (k_{eff})	Computation Time (Min)
600	0.9983	2.818
700	0.9988	3.102
800	0.9989	3.592
900	0.9990	3.729
950	0.9990	3.845
1000	0.9990	4.282

4.1.2. Mesh size optimization

Having established the optimal number of iteration, the effects of the mesh size on the computation is examined in this section. The Table 2 reveals that the values of k_{eff} increases as the mesh sizes becomes smaller until an optimal mesh size of 1 x 1 cm² is reached and further decrease in mesh sizes gives no further improvement in the value of k_{eff} .

Table 2. Mesh size optimization and its corresponding maximum effective multiplication factor (k_{eff}) with constant 1000-iteration.

Mesh Size Area (cm ²)	Effective Multiplication Factor (k_{eff})	Computation Time (Min)
4 x 4	0.9990	4.282
2.4 x 2.4	0.9992	6.015
2 x 2	0.9996	6.751
1 x 1	0.9998	7.393
0.8 x 0.8	0.9998	8.491
0.5 x 0.5	0.9998	9.553

4.2. Neutron Flux Profile

The neutron flux profile was considered for both the axial and radial (3D) directions. This approach gave a better understanding of the behaviour of the neutron flux in the cylindrical reactor core. Comparing the results of the neutron flux distribution in the radial and axial directions obtained from TUNTOB with that of the neutron flux distribution of THESIS Code (Harman, 2001). It was observed that TUNTOB obtained better results than the THESIS Code, although, not all the THESIS source code parameters were accessible. In addition, we observed that the graphs of the THESIS Code follow the same trend with that obtained in this study.

4.2.1 Neutron flux distribution in 3-D representation

The color difference or variation in the neutron flux distribution for the 4 by 4 mesh from group 1 to group 4 confirms that the centre of the core has the greatest amount of heat (and the neutron flux has the highest value at the centre of the core) and the heat gradually reduces as the neutron flux moves away from the centre of the core until it gets to the surface of the core (from

color red, changes to color yellow and a light green color and then to color blue). The same trend occurs for other different mesh sizes for the four-group.

The neutron flux distributions in 3-D representation are shown in Fig. (4-11). The figures describe the behavior of the neutron flux for the four groups in both the radial and axial directions. The neutron flux profile showed that all the group behave in the same manner having maximum values at the center of the reactor core, ($r = 0, z = H/2$). The neutron flux for the first group (Group 1) has the highest maximum value, followed by the second (Group 2) and third group (Group 3) while the fourth group (Group 4) has the lowest. This trend is expected because fission neutrons are produced directly into the first three groups and the scattering of neutrons from these three groups serves as the source of neutrons in the fourth group. In Fig. (4-11), the 4 by 4 mesh showed that the trend of the flux in between the mesh points follows straight lines but when the number of mesh points is increased, the trend becomes a smooth curve as shown in Fig. (4-11) for a 1 by 1 mesh. It is expected that further increase in the number of mesh points will produce smoother curves with a corresponding increase in the computational time.

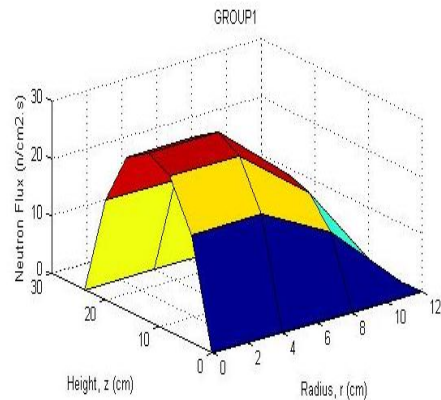


Fig. 4. Neutron flux distribution in 3D for the first group of a 4 by 4 mesh.

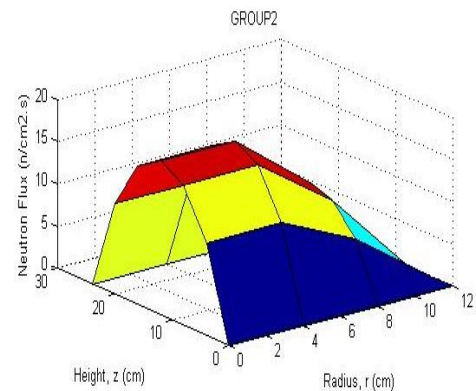


Fig. 5. Neutron flux distribution in 3D for the second group of a 4 by 4 mesh.

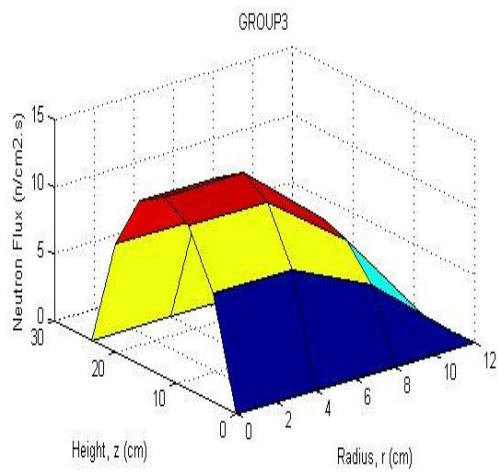


Fig. 6. Neutron flux distribution in 3D for the third group of a 4 by 4 mesh.

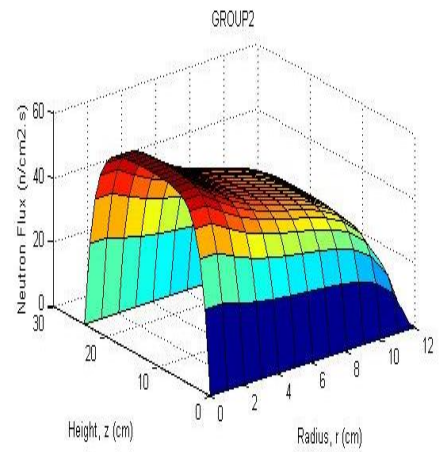


Fig. 9. Neutron flux distribution in 3D for the second group of a 1 by 1 mesh.

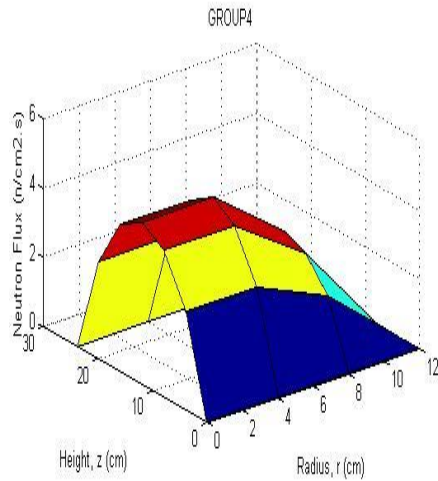


Fig. 7. Neutron flux distribution in 3D for the fourth group of a 4 by 4 mesh.

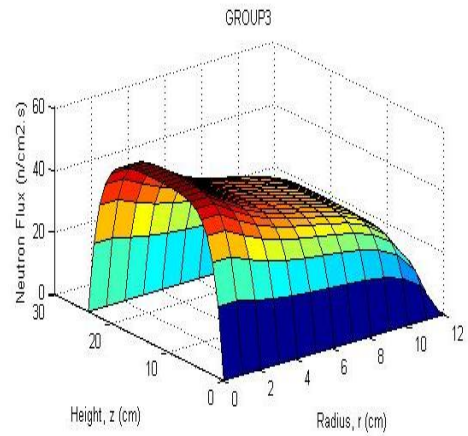


Fig. 10. Neutron flux distribution in 3D for the third group of a 1 by 1 mesh.

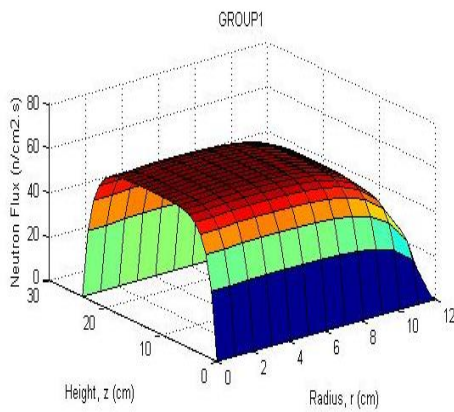


Fig. 8. Neutron flux distribution in 3D for the first group of a 1 by 1 mesh.

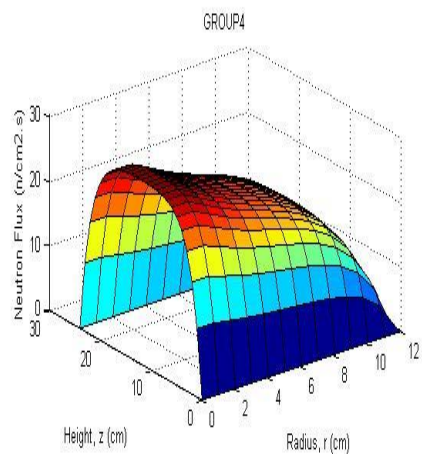


Fig. 11. Neutron flux distribution in 3D for the fourth group of a 1 by 1 mesh.

In this work, we have derived four group diffusion equations for a cylindrical reactor core which gives a detailed description of neutron distribution in the core. We derived the discretized four group diffusion equations for a cylindrical reactor core because it gives an exact description of what takes place in a low water reactor (LWR). The results obtained for the criticality calculations were compared with criticality benchmarks and found to be very close. For instance, the k_{eff} calculated by the code is found to be 1.246728 while the benchmark value is 1.246368 (Ganapol, 2014).

CONCLUSION

This study provides the criticality calculation and neutron flux distribution in a homogenous cylindrical reactor core in two dimensions (r, z) using four energy groups. From the results these studies further confirm that the centre of the core of the reactor has the greatest heat which is synonymous to the different colour variations relating to decrease in the amount of heat as it moves away from the centre of the core. The calculations were carried out for a reactor in a steady state. The developed algorithm (TUNTOB), calculates values of k_{eff} and the neutron distribution as a function of the mesh sizes. It was found that the accuracy in the value of k_{eff} and the smoothness of the neutron distribution curves in 3-D representations, depends on the number of mesh points. It allows the user to modify the reactor dimensions and see the impacts on the neutron distribution and criticality within the reactor core.

ACKNOWLEDGEMENT

Authors wish to acknowledge the support provided by the Department of Physics and Engineering Physics, the Center for Energy Research and Development, and the Department of Electronic and Electrical Engineering, Obafemi Awolowo University, Ile-Ife, Nigeria.

REFERENCE

Atomic Energy Control Board of Canada, *Fundamental of Power Reactors*. Canada: Atomic Energy Control Board of Canada (AECBC), pp. 1-3, 1993. Available [online]: <http://www.thecanadianencyclopedia.ca/en/article/atomic-energy-control-board/>

A. Arzhanov, *Analytical Models of Critical Reactor in Simple Geometries*, Royal Institute of Technology, Department of Physics. Stockholm, Sweden: KTH Engineering Sciences, pp. 1-33, 2010.

B. Ganapol, *Verification of the CENTRM Module for Adaptation of the SCALE Code to NGNP Prismatic and PBR Core Designs*, University of Arizona. Arizona: Reactor Concepts RD and D, 2014.

D. B. Ganapol, *The Analytical Solution to the Multigroup Diffusion Equation in One - Dimensional Plane, Cylindrical and Spherical Geometries*, *Joint International Tropical on Mathematics and Computation and Supercomputing in Nuclear Application*, 2007.

J. D. Burnham, *Reactor Theory - The Steady State*, *Nuclear Training Course*, 1967.

J. J. Duderstadt and J. L. Hamilton, *Nuclear Reactor Analysis*. Michigan: John Wiley and Sons, Inc, 672p, 1976.

J. T. Urbatsch, *Iterative Acceleration Methods for Monte Carlo and Deterministic Criticality*. California: Los Alamos National Laboratory, pp. 1-174, 1995. Available [online]: <https://www.osti.gov/scitech/servlets/purl/212566>

J. Kiusalaas, *Numerical Methods in Engineering with Matlab*, New York: Cambridge University Press, pp. 1-435, 2005.

M. A. Jayeola, M. K. Fasasi, A. A. Amosun, A. O. Salau, B. M. Ojo (2018), Numerical Computation of Fission-Product Poisoning Build-up and Burn-up Rate in a Finite Cylindrical Nuclear Reactor Core, *Bilge International Journal of Science and Technology Research*, Vol. 2(1), pp. 17-30.

M. S. Stacey, *Nuclear Reactor Physics*. Atlanta: Wiley-Vch Verlag GmbH and Co. KGaA, Weinheim, 735p, 2007.

R. J. Larmash and J. A. Baratta, *Introduction to Nuclear Engineering (3rd edition)*, New Jersey, 420p, 2001.

T. Tanbay and O. Bilge, Numerical Solution of the Multigroup Neutron Diffusion Equation by the Meshless RBF Collocation Method, *Mathematical and Computational Applications*, Vol. 18, pp. 399-407, 2013.

W. H. Harman, *Modelling Pressurized Water Reactor Kinetics*, Ohio, Wright-Patterson Air Force Base, 2001.

Copyright © Turkish Journal of Engineering (TUJE). All rights reserved, including the making of copies unless permission is obtained from the copyright proprietors.



CONTENTS

- RHEOLOGICAL PARAMETER ESTIMATION OF CMC-WATER SOLUTIONS USING MAGNETIC RESONANCE IMAGING (MRI)
G. Bengusu Tezel..... 94
- INVESTIGATION OF Ni-Mn BASED SHAPE MEMORY ALLOY VARIATIONS TRANSFORMATION TEMPERATURES
Ece Kalay, Anil Erdağ Nomer and Mehmet Ali Kurgun 98
- INVESTIGATION OF DISSOLUTION KINETICS OF Zn AND Mn FROM SPENT ZINC-CARBON BATTERIES IN SULPHURIC ACID SOLUTION
Tevfik Agacayak and Ali Aras 107
- COMPARATIVE STUDY OF REGIONAL CRASH DATA IN TURKEY
Murat Özen..... 113
- PERFORMANCE COMPARISON OF ANFIS, ANN, SVR, CART AND MLR TECHNIQUES FOR GEOMETRY OPTIMIZATION OF CARBON NANOTUBES USING CASTEP
Mehmet Acı, Çiğdem İnan Acı and Mutlu Avcı..... 119
- INVESTIGATION OF ULEXITE USAGE IN AUTOMOTIVE BRAKE FRICTION MATERIALS
Banu Sugözü 125
- CRITICALITY CALCULATION OF A HOMOGENOUS CYLINDRICAL NUCLEAR REACTOR CORE USING FOUR-GROUP DIFFUSION EQUATIONS
Babatunde Michael Ojo, Musibau Keulere Fasasi, Ayodeji Olalekan Salau, Stephen Friday Olukotun and Ademola Mathew Jayeola..... 130

ISSN 2587-1366

TURKISH JOURNAL OF ENGINEERING